An Environmental Monitoring Device to Identify Potential Risks for Intraventricular Hemorrhage During Neonatal Transport of Preterm Infants

Carlos E Guevara

Thesis submitted to the faculty of the Virginia Polytechnic Institute and State University in partial fulfillment of the requirements for the degree of

Master of Science

In

Mechanical Engineering

Alfred L Wicks (Chair)

Kathleen Meehan

Andre A Muelenaer

November 3, 2011

Blacksburg, Virginia

Keywords: Intraventricular Hemorrhage, Neonatal Transport, Preterm Infants

An Environmental Monitoring Device to Identify Potential Risks for Intraventricular Hemorrhage During Neonatal Transport of Preterm Infants

Carlos E Guevara

ABSTRACT

Purpose: To characterize the environment in both ground and aerial ambulances in an effort to identify and quantify the risk factors associated with intraventricular hemorrhage (IVH) in preterm infants, with the goal of developing a device to mitigate this problem.

Methods: A small, stand-alone battery operated device was developed to characterize the environment inside neonatal transports. This device included an array of sensors to measure acceleration forces, sound levels, temperature, pressure, and light intensities. Two of the data acquisition devices were used to collect data inside and outside the transport incubator simultaneously for a period of thirty minutes during a test flight in a transport helicopter. Real-time digital signal processing was performed for the sound signals to reduce data. Furthermore batch digital signal processing was performed on an external computer to calculate the vibration spectrograms, occurrence of impulsive forces, and variations in ambient temperature, pressure and luminance. The results were compared between the two devices to determine whether the current transport incubator design is reducing or increasing the suspected risk factors.

Results: The vibration levels registered in the transport incubator during flight were five times greater than in the crew cabin in the vertical direction. High vibration levels were registered in the horizontal direction in the transport incubator, which were not registered in the crew cabin. In contrast, vibration in lateral direction was nearly half of that registered in the crew cabin. Sound levels were on average 70 dBA in the transport incubator. Luminance levels reached values up to 6920 Lux. No major changes in temperature and pressure were registered.

Conclusions: IVH is a serious consequence of transporting preterm infants from one health care facility to another and occurs in roughly one out of three infants. To address this problem, a transport monitoring device can help characterize the environment in these transports in an effort to design a new state of the art transport incubator to mitigate this problem.

Acknowledgements

I thank my advisor Dr. Alfred Wicks for his support and advice, for helping me think outside the box, and for being like a father figure to me here in the United States.

I thank Dr. Muelenaer, member of the Carilion Clinic Children's Hospital, for his help in guiding me to the right people and for his diligent support in the medical side of this project.

I thank Dr. Meehan for her support and input in the electrical engineering side of this project.

Special thanks go to Susan M. Smith, Program Director of Carilion Clinic Life-Guard, Paul B. Davenport, Vice President-Emergency Services, and the entire Carilion Clinic Patient Transport crew for dedicating their valuable time into this project. The completion of this research would have not been possible without their help.

I thank Dr. Anuj Sinha and the Pediatrix Medical Group for guiding me into this research and for their help in leading me to others who were interested in this project.

I thank Jackie Martin, member of the Carilion Clinic Children's Hospital for her input on the literature review section of this research.

I thank my parents for their support and for always being there for me; even from far away.

I thank the members of the Mechatronics Lab at Virginia Tech for their friendship and support through the difficult times. Special thanks go to Dr. John Bird for helping me think outside the box. I would have not been able to this without all of your help!

I thank Brandy McCoy for her exhaustive help throughout my time as a graduate student at Virginia Tech

I want to thank Kristin DallaPiazza, my best friend, for all of her emotional support. Thank you for helping me appreciate life and for helping me understand what is important. Also, thank you for your help and patience through this long journey. I finally did it!

Table of Contents

List of Figures

List of Tables

Chapter 1: Introduction

Premature babies are those born before 37 weeks of gestational age (GA) and are at a higher risk for mortality and morbidity than term newborns [1]. Prematurity is a serious health risk for newborns and is also the main cause of death in this population [1]. Preterm infants usually require special care and tend to spend weeks, even months, hospitalized in a neonatal intensive care unit (NICU) [1]. In the United States, more than half a million babies are premature [1]. That is, 12 % of all newborns are premature and will require special care from the NICU to survive [1, 2]. The survivors are likely to face developmental consequences such as respiratory problems, cerebral palsy, and mental retardation [1, 3]. These consequences may be attributed to the most common morbidity in this population, which is intraventricular hemorrhage (IVH) [3, 4].

IVH results from the rupture of blood vessels in the ventricles of the brain, which produces bleeding that may extend into the brain tissue. IVH is the most common and most dangerous disease within premature babies and occurs in between 10 and 40 percent of all preterm infants, and in 33 percent of preterm infants who require transport to a higher level health care facility [4-6]. Based on a study in Germany, 44 percent of the babies who develop IVH Grade III and Grade IV died [7]. IVH is diagnosed via intracranial ultrasound and is classified into four grades [8]. Grades I and II IVH are considered mild IVH and are recognized when hemorrhage extends as far as the ventricles and partially fills them [8]. Generally, preterm infants who develop either grade I or II IVH recover and this injury does not present consequences in the long run. In contrast, grades III and IV IVH are considered severe IVH where the hemorrhage dilates the ventricles and, in the most severe case, ruptures through the ventricles into the brain tissue [8]. Severe IVH results in serious long term consequences such as cerebral palsy, mental retardation, or death [3]. The consequences of severe IVH are not only medical, but also economic; 3600 new cases of mental retardation due to IVH are presented each year, with costs that may exceed 3.6 billion dollars in medical care expenses throughout their life span [9].

The mechanism that triggers IVH is a combination of the neuroanatomical, physiological and environmental risk factors. Risk factors for IVH at the neuroanatomical level include high cerebral blood flow and blood pressure, brain tissue composition, maturity of the germinal matrix, and blood vessel and arterial structure [4]. High cerebral blood flow and blood pressure may be triggered by common physiological insults such as hypothermia and asphyxia. At the physiological level, risk factors for IVH include GA under 32 weeks and body weight under 1,500 grams. There is a strong correlation between younger and smaller premature babies, and higher cerebral blood pressure, higher cardiac demands, and a higher fibrinolytic activity [4]. Physical stressors are the main environmental risk

factors, which generally arise from the NICU environment and the need to transport preterm infants from one health care facility to another. These physical stressors include acceleration forces with or without direct impact, high noise levels, sudden drops in ambient temperature, changes in barometric pressure, and the presence of bright or flickering lights. On average, while the IVH incidence for all inborn preterm babies has decreased over the past three decades, the IVH incidence on those babies who require transport has remained at roughly 33 percent [3].

Premature infants who are transported from one health care facility to another are at higher risk of developing IVH. In a series of studies, 33 percent of babies who required transport to another health care facility developed IVH [5, 6, 10]. Forty four of the babies who developed Grade III and Grade IV IVH died [7]. The transport environment is of particular interest because it not only exposes the premature babies to direct physical stressors such as acceleration forces and loud noise, but also to those indirect stressors such as changes in temperature, pressure, and light intensities, which have been shown to accelerate their cardiac rhythm [11].

Previous research on the quantification of physical stressors during transport show that acceleration forces up to 0.9 G's and noise levels up to 93 dB were measured in a helicopter [12, 13]. In contrast, acceleration forces up to 0.9 G's and noise levels up to 67 dB were measured in a ground ambulance [12, 13]. Measurements were made from within the neonatal transport incubator for both vehicles. In adults, high acceleration forces increases cardiac demands and acceleration forces above 5 G's induces unconsciousness from decreased cerebral blood flow [14]. Very high sound levels are not only stressful and painful, but can also cause moderate traumatic brain injury by propagation of the sound wave through the thoracic cavity [15]. It is safe to assume that the thresholds for premature babies are much lower than those for adults and the consequences of such stressor may be far more devastating.

The objective of this research was to characterize the environment in both ground and aerial transport vehicles in an effort to identify the risk factors associated with IVH. The approach was to use two small, battery powered environmental monitoring devices to monitor the environment. One monitoring device was placed inside the neonatal transport incubator and the other was placed inside the vehicle but outside the incubator. The goal of this approach was to develop an experimental model for the incubator and to discover any potential risk factor that may be induced or magnified by the incubator. Each monitoring device consists of a sensor array which measures acceleration forces, noise levels, temperature, pressure, and light intensities. A microprocessor collects data from the sensor array, processes the acoustic noise data in real time, and stores the consolidated data into an external memory card. Spectrograms were created to present the mechanical vibration and acoustic noise data and histograms were created to present the occurrence of short duration and high magnitude acceleration forces. Temperature,

pressure, and light intensity data are presented on plots which show the mean value, maximum value, and variance of the measurements over the duration of the transport.

The expected outcome of this research was to validate the data acquisition device and to obtain a preliminary understanding of the environment that premature babies are exposed to during transport. This research took the work by the authors mentioned in this document one step further. A better understanding of the acceleration forces and acoustic noise frequencies will help us identify the source or sources of the physical stressors. Also, taking measurements inside and outside of the neonatal transport incubator will help discover what the incubator is doing well to protect the infant and what improvements can be made in order to develop a device to mitigate the IVH problem in neonatal transports.

Chapter 2: Literature Review

2.1 Introduction

This review emphasizes the research done in the past thirty years that pertains to IVH in preterm infants. The definition, incidence, diagnosis, and consequences of IVH are covered in this review, and are followed by the risk factors that lead to this morbidity. Of particular interest are the environmental factors that preterm infants experience during transport. The closing section covers the work done by various researchers that attempted to identify environmental risk factors in both NICU's and neonatal transports.

2.2 Definition of Intraventricular Hemorrhage

According to Perlman and Volpe, IVH is most common in preterm infants and has been considered the most dangerous cause of morbidity among this population [4, 16]. IVH is defined as bleeding that originates from the small capillary blood vessels in the sub-ependymal germinal matrix which extends into the ventricles inside the brain. This condition is the result of alterations in the cerebral blood flow, rupture of the capillary vessels in the brain due to concussions, or a combination of both. In newborns, the bleeding originates from the choroid plexus, and, in very premature infants (under 28 weeks of gestational age), the bleeding originates from the head of the caudate nucleus [4, 16].

The severity of the hemorrhage is most commonly classified into four grades or four corresponding classes and is determined by the progression of the blood into the ventricular system [8, 17]. Grade I [8, 18] or mild IVH [17] occurs when the bleeding is limited to the sub-ependymal germinal matrix. Grade II [8, 18] or moderate IVH [17] occurs when the hemorrhage ruptures through the ependymal matrix and extends to about 50% of the ventricles. Grade III [8, 18] or severe IVH that forms a cast in the ventricle [17] occurs when the hemorrhage does not stop and continues to fill the ventricles. Grade IV [8, 18] or severe IVH with intra-cerebral extension [17] occurs when the bleeding dilates the ventricles and ruptures into the brain tissue. For the remainder of this document, the grade classification of IVH will be used.

2.2.1 Incidence

IVH is a common but deadly disease among newborns who are less than 32 weeks of gestational age and who weigh less than 1.5 kg [4]. The fact that the brains of the

neonates are fragile and underdeveloped makes them particularly susceptible to injury. Approximately 40 to 45 percent of inborn neonates admitted to the NICU, a facility that offers specialized emergency care for neonates, are diagnosed with IVH [4]. The risk of morbidity may increase to 70% for those requiring mechanical ventilation [18]. Favorably, improved neonatal care has reduced the overall incidence over the past 30 years. Eighty percent of the neonates diagnosed with grade I IVH are at risk of evolving to grades II, III, or IV of IVH [4]. Since IVH is most common in neonates, it is important to consider them at high risk and, therefore, repetitive ultrasound scans of their head are highly recommended. Table 2-1 shows the results, arranged in chronological order, of various studies regarding the detection and prevention of IVH in newborns who are less than 32 weeks gestational age (GA) over the last 30 years.

Table 2-1. Summary of the results found in the last 30 years [3-7, 10, 19-22]

Year	Author (s)	BW < 1.5 Kg	All IVH	% incidence	IVH III and IV	OB IVH	% incidence due to transport	OB IVH III and IV
1981	Volpe et al. [4]	Yes		40 – 45				
1982	Levene et al. [19]	No	52/146	35.6	11/146	30/50	60.0	
1992	Yoder et al. [6]	Yes	26/81	32.1	6/81	21/58	36.2	9/58
1997	Shlossman et al. [10]	No				18/88	20.5	
1999	Mancini et al. [3]	Yes	20/67	29.8	6/67			
2000	Towers et al. [20]	Yes			37/329			10/44
2000	Gleissner et al. [7]	Yes	136/3649	3.7		83/1125	7.4	
2001	Hohlagschwandtner et al. [21]	No	61/225	27.1	26/225	7/34	20.6	4/34
2002	Koksal et al. [5]	Yes	18/120	15.0		10/28	35.7	
2010	Lee et al. [22]	Yes	290/1044	27.8				

The data shows that, while the overall risk for IVH has dramatically declined over the last 30 years, the risk for IVH in the neonate population who require transport remains relatively high. These results suggest that, while neonatal care has significantly improved over the last few decades, very little improvements have been achieved to reduce the risk for IVH for those preterm infants requiring transportation from one health care facility to another after birth.

2.2.2 Diagnosis

The two most common methods for diagnosing IVH are ultrasound scans and computed tomographic (CT) scans. The ultrasound scan consists of placing a piezoelectric transducer on the forehead or on the side of the head to obtain images from the coronal or sagittal planes, shown in Figure 2-1 and Figure 2-2, respectively. Ultrasonic waves, typically in the 5 MHz range, travel into the head, and are reflected back to the transducer [4]. Figure 2-1 shows an image of the ventricles as seen from the front of the neonate and clearly shows the left ventricle flooded with blood. Similarly, Figure 2-2 shows an image of the left side of the neonate's head and the corresponding damaged ventricle.

Figure 2-1. Ultrasonic image of the Coronal plane [4]

Figure 2-2. Ultrasonic image of the Sagittal plane [4]

A CT scan system pass x-rays through the head and measures the difference between the emitted rays and the received rays. Figure 2-3 shows a typical axial CT scan of the patient's head; blood is represented by white opacities inside the ventricles.
Figure 2-4 shows a frontal CT scan that shows the flooding of blood in the left ventricle.

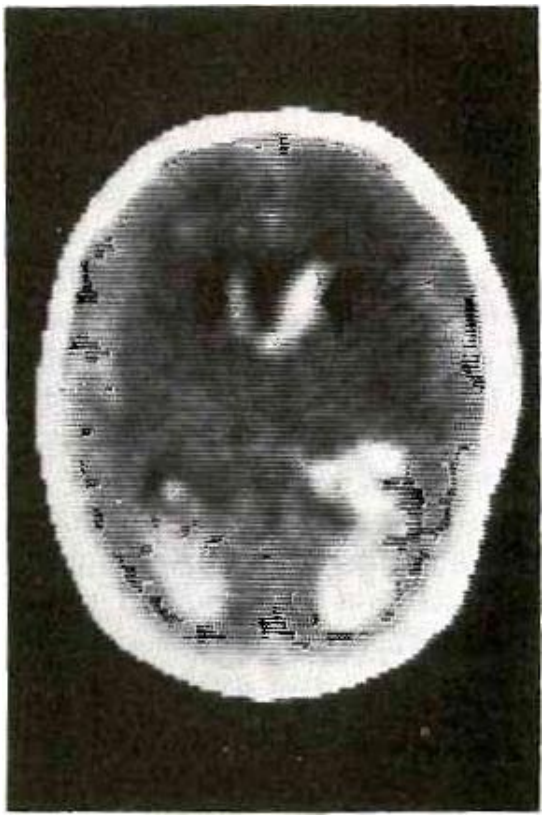

Figure 2-3. Axial CT scan of the head [4]

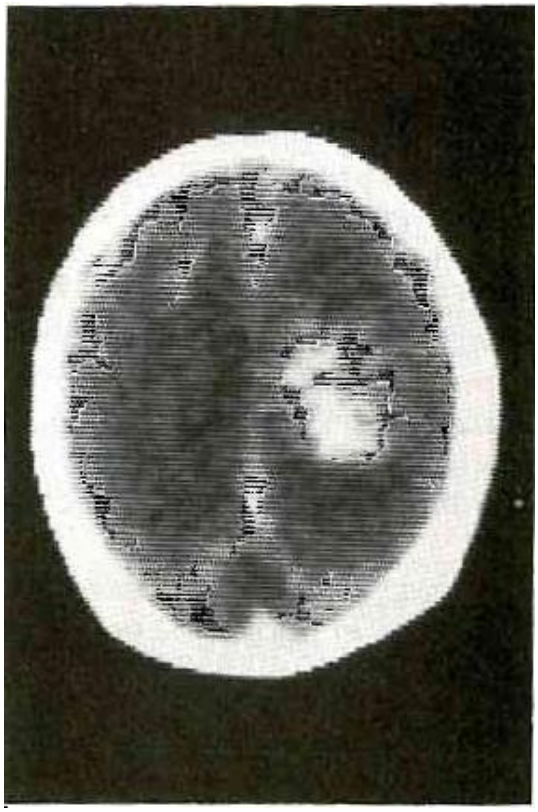

Figure 2-4. Frontal CT scan of the head [4]

CT scanning is a very accurate method for detecting IVH; however, the device is not portable and the effects of both the constant movement and the radiation on the already ill neonate are still unclear [4]. Ultrasound scanning is the preferred diagnostic method because it is safe and portable and the accuracy of the diagnosis is equivalent to that of the CT scan [4]. For all the IVH diagnoses reported on the literature review of this document, IVH was diagnosed by means of cranial ultrasound.

2.2.3 Developmental Consequences

The short term consequences of IVH are apnea crisis, post hemorrhagic hydrocephalus, and periventricular leukomalacia. More serious consequences of IVH are mental retardation, cerebral palsy, a combination of both, or death [3]. Currently, an average of 20 – 25% of very low birth weight neonates develop IVH, of which 10 -15% are more severe, and 75% of those with severe IVH develop mental retardation and/or cerebral palsy. Based on national data, over 3,600 new cases of mental retardation are attributed to

IVH in the United States each year [9]. In addition, the lifetime care cost for all 3,600 children may exceed 3.6 billion dollars [9].

2.3 Risk Factors Associated with Intraventricular Hemorrhage

This section covers the risk factors associated with IVH which have been studied for over two decades. To describe a complete understanding of causes of IVH, we begin with the most internal possible source of IVH which is fluctuation in blood flow and blood pressure associated with the intravascular pressure. The extravascular environment associated with IVH includes tissue composition and the maturity of the germinal matrix as well as blood vessel and arterial structure. Outside of the neuroanatomy are the perinatal factors that are directly related to the physiology of the preterm infant. Finally, the environmental factors that the preterm infants are exposed to after birth are discussed in great detail.

2.3.1 Neuroanatomical Factors

The neuroanatomical factors relative to preterm infants include intravascular pressure, vascular integrity, and extravascular environment. Together, these factors influence the overall blood flow regulation and circulation in the periventricular region of the brain [4].

In the preterm infant, an increased blood supply carried by the blood vessels to the ependymal matrix, suggest that an irregular amount of blood enters the periventricular region or white matter. Therefore, any alterations in the neonates' blood flow tend to elevate the pressure even more in the periventricular region [4]. Figure 2-5 shows the location of the white matter and the location of the germinal matrix, which is a gelatinous structure that provides support to the capillaries represented by the red objects.

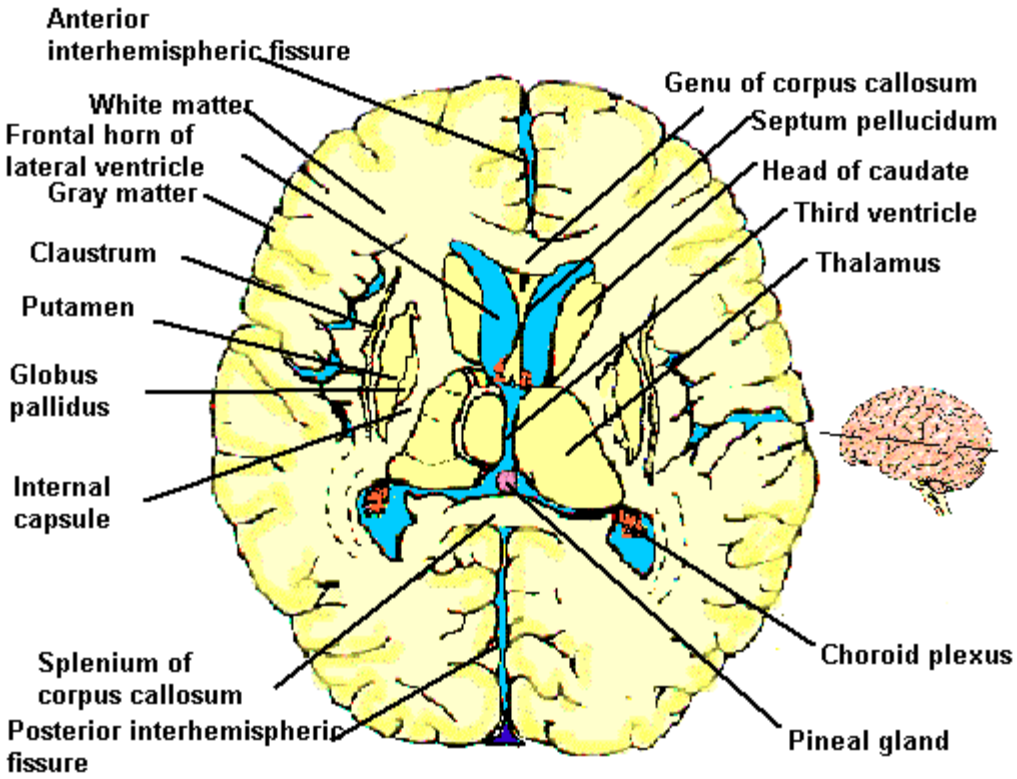

Figure 2-5. Top view of the human brain anatomy

Increases in cerebral blood flow may arise from insults such as asphyxia [9]. Also, elevated venous pressure may contribute to elevated blood pressure in the capillary bed as a result of asphyxia. This elevated blood pressure in the capillary bed generally occurs at the level of the foramen of Monro and the head of the caudate nucleus, because, as shown in Figure 2-6, this region's anatomy is characterize by a sharp U-turn in the direction of flow [4]. Since auto regulation of the blood flow is shown to be impaired in this infant population, the periventricular region is extremely sensitive to changes in arterial blood pressure; in fact, increases in cerebral blood flow and arterial pressure have been observed during the first minutes post-delivery [4].

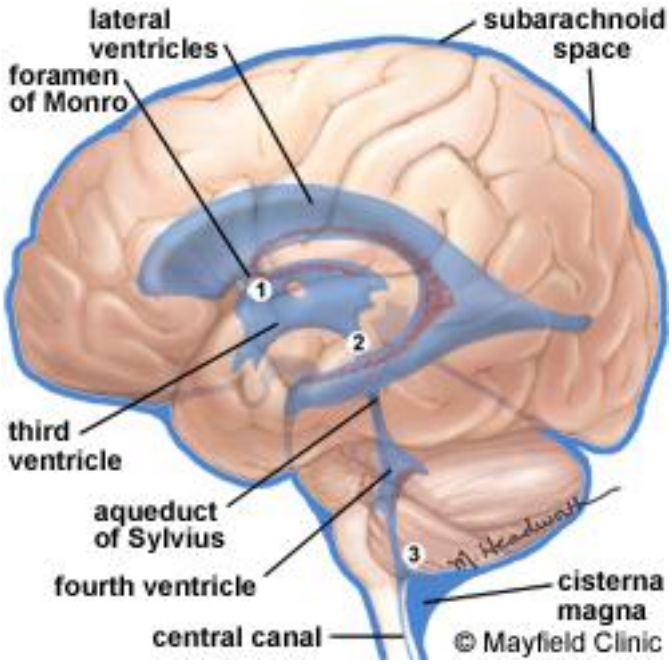

Figure 2-6. Cerebral ventricular system. Used with permission from Mayfield Clinic

Moreover, anatomic observations suggest that the vascular integrity of the capillary bed in the germinal matrix is immature, making it fragile and very susceptible to rupture upon hypoxic events [4].

The periventricular region is composed of the sub-ependymal germinal matrix, which is known as a gelatinous region that provides poor support to the small blood vessels in it [4]. Since this germinal matrix does not dissipate in the fetus until term, it provides very poor support to the small capillary vessels within it. Thus, this poor support increases the preterm infant's vulnerability of bleeding of the capillaries [4]. In addition, this region contains high fibrinolytic activity, an activity that enables enzymes to dissolve the fibrin in blood coagulates is more prominent in babies between 22 to 30 weeks gestational age [23]. According to Gilles et al. [23], plausible inhibitors of this activity include physical exertion and administration of adrenalin. The increased fibrinolytic activity in babies between 22 and 30 weeks gestational age explains why bleeding from the capillaries is very likely to extend into a massive hemorrhage in the ventricles [4].

2.3.2 Physiological Factors

A study conducted by Gleissner et al. [7] identified young gestational age, small for gestational age, male gender, respiratory distress syndrome, low blood pH, low body temperature, and intubation after birth as the major potential physiological risk factors for IVH. Results showed that the highest physiological risk factors, from most to least significant, were gestational age below 28 weeks, intubation after birth, and body temperature below 35 ºC. Gender and blood pH were associated with no significant risk

for IVH [7]. Table 2-2 summarizes Gleisser's et al. results related to the physiological risk factors.

Table 2-2. Risk for IVH according to gestational age, body temperature, and intubation after birth [7]

Risk factor	# of patients	# of IVH cases	% of IVH
Weeks of gestational age			
23 - 27	166	66	48.5
28 - 31	470	44	32.4
32 - 36	3011	26	19.1
Intubation after birth	522	109	80.1
Body temperature ≤ 35 ºC	118	96	70.6
Total	3649	136	

The cases of IVH in Gleisser's study include all grades of IVH. As shown by this study, preterm infants born at less than 30 weeks of gestational age are at the highest risk because of their underdeveloped brains, their inability to self-regulate arterial and venous pressure, and their high fibrinolytic activity. On the contrary, intubation after birth presented an increased risk among preterm infants between 32 to 36 weeks gestational age than in infants between 23 to 27 weeks gestational age [7]. Low body temperature presented the same level of risk for all age groups. In addition, Koksal et al. [5] have reported that respiratory distress syndrome (RDS) along with the artificial ventilation to treat RDS increase cerebral venous pressure and may cause some fluctuation in the blood flow. The discussion chapter of this report addresses in detail the effects of artificial ventilation and the risk for IVH.

2.3.3 Environmental Factors

After birth, the preterm newborn is exposed to an environment for which he or she is not yet prepared for. The environmental factors of most significance in this research are those related to transporting the neonates from one healthcare facility to another. A study conducted by Hohlagschwandtner et al. [21] compared the probability of mortality and morbidity between antenatal transported infants (ATI), postnatal transported infants (PTI), and preterm inborns (NTI) delivered at the University Hospital of Vienna. Results showed a significantly higher risk for severe morbidity in the PTI group of 11.8% compared to 5.5% in the ATI group; however, a total of 17.7% of the PTI group suffered from either mild or severe morbidity. The probability for severe morbidity in the PTI group would have been even higher had they included infants who passed away and were

regarded as “non-viable” for transport [21]. No significant risk was present in the NTI group. Towers et al. [20] examined the incidence of grade III and grade IV IVH by comparing premature babies who weighted between 500 and 1,200 g and were at least 24 weeks GA, but were born in different facilities. They compared newborns delivered at level III healthcare institutions with outborn babies who were transported from a level I to a level III facility. Their results state that out of the 329 babies studied for the incidence of IVH, 9% of the 285 inborns developed grade III or IV IVH as compared to the 23% of the 44 outborns who suffered the same lesions [20]. While both studies present different results due to their criteria when selecting study groups, they still highlight the increased risk of transporting a preterm infant as compared to those delivered in the higher level institutions.

Shah et al. [14] attempted to quantify the impulses experienced by neonates during intra hospital transport. This study aimed at quantifying the accelerations experienced by premature babies during transport by attaching an accelerometer to the forehead of a neonatal resuscitation mannequin. Five trials were conducted for this study utilizing a standard ambulance and a transport incubator. They reported that up to 3G’s were experienced by the mannequin during a 10 minute ambulance transport [14]. The significant consequences that arise from experiencing high acceleration levels are not only the direct trauma to the germinal matrix due to the transport induced forces, but also the increased likelihood of extubation due to these forces [14].

Mori et al. [24] analyzed the effect of the duration of the transport on mortality and morbidity. Results show that for inter facility transports lasting longer than 60 minutes, the risk for death was 12% to 30% higher than that of those whose transport lasted less than 60 minutes. Also, longer transport times compromised body temperature control and resulted in an increased risk for neonates to develop IVH [24].

Li et al. and Kellam et al. quantified the effects of noise levels and assessed a sound spectral analysis inside NICU’s. They found unwanted acoustical stressors, especially noise levels above 70 dB and above 500 Hz, increase the risk for IVH from 21% to 41% [25, 26]. Bremmer et al. added that these unwanted stressors interfere with the neonates’ medical, behavioral, and developmental stability and usually produce harmful physiological effects such as elevated blood pressure, elevated heart rate, and hypoxia [27]. As stated in the neuroanatomical risk factors section, these conditions may increase the risk for developing IVH.

Antonucci et al. found other environmental factors, such as temperature and light intensity, indirectly increase the risk for IVH by disrupting the neonates’ physiology [11]. It was observed that the neonates’ larger skin surface area-to-body mass ratio compromised their ability to maintain their normal body temperature, mostly due to heat losses by means of radiation and evaporation [11]. Unlike term newborns, thermoregulation for neonates is more complex and results in a much narrower thermal

neutral zone, where the neonates may regulate body temperature near normal without increasing their metabolic rate [11]. If their body temperature falls just below the neutral zone, they compensate by increasing their metabolic rate and oxygen consumption [11]. If their body temperature drops even more, they begin to experience hypothermia, increased oxygen and glucose requirements, and higher metabolic acidosis in the blood-stream [11]. Additionally, bright light exposure, as compared to the warm, dark environment present inside the mother's womb, adversely affects the neonates' comfort [11].

2.4 Previous Studies in the Identification and Quantification of Environmental Risk Factors for IVH

The results found by Bremmer and Antonucci in their noise measurements in the NICU are summarized in Table 2-3.

Table 2-3. Noise levels measured in the NICU [11, 27]

Investigator (s)	Source of Noise	Decibel Level
Bremmer et al.	Conversation between nurses	50
	Bradycardia alarm	55 – 88
	Conversations	58 – 64
	Using incubator top for writing	59 – 64
	IV pump alarm	61 – 78
	Turning sink on and off	66 – 76
	Opening plastic sleeve of incubator	67 – 87
	Closing incubator cabinet	70 – 95
	Closing a solid incubator porthole	80 – 111
	Dropping head of mattress	88 – 117
	Placing bottle on top of incubator	96 – 117
	Banging incubator to stimulate infant	130 – 140
Antonucci et al.	Human-related source	Up to 80
	Incubator motor	74 - 80

Adapted from Bremmer (2003) and Antonucci (2009) [11, 27]

Both studies agree in that the largest contributors to the high noise levels in the NICU are due to the staff personnel. The consequences result in negative physiological responses such as increased heart rate, increased respiratory rate, and decreased blood oxygen saturation. Suggestions for decreasing the noise levels include minimizing the conversation between staff members and installing sound absorbing material around the NICU.

Sitting and Bouchut conducted similar studies but inside neonatal transports as compared to earlier studies in the NICU [12, 13]. Their results have been summarized in Table 2-4.

Table 2-4. Noise levels inside both ground and aerial neonatal transports [12, 13]

Investigator (s)	Instrumented Vehicle	Noise in Crew Cabin (dB)	Noise in Incubator (dB)
Sitting et al. (2011)	BK – 117 aircraft	90	93
	King Air B200 aircraft	84	78
	Pilatus PC – 12 aircraft	86	80
	Bell 222 aircraft	88	82
Bouchut et al. (2011)	EC135 Eurocopter		86
	Renault Master van		67

Adapted from Sitting (2011) and Bouchut (2011) [12, 13]

The result shows that the noise levels inside the aerial transport are much higher than those in the ground transport. However, Bouchut's study shows that there was a lower fluctuation of the sound level in the aerial transport as compared with the ground transport [13].

An effort to quantify the magnitude of vibration and g-forces inside neonatal transport vehicles is evident by studies conducted by Shah and Bouchut [13, 14]. The results are summarized in Table 2-5.

Table 2-5. Vibration levels and g-forces measured in both ground and aerial neonatal transports [13, 14]

Investigator (s)	Instrumented Vehicle	Front to Back Acceleration (m/s^2)	Side to Side Acceleration (m/s^2)	Vibration (m/s^2)
Shah et al. (2008)	Standard medical ambulance	39*	22*	9*
Bouchut et al. (2011)	Renault Master van	0.9		0.49
	EC135 Eurocopter	0.88		1.0

*Measurements made by attaching accelerometer to a resuscitation mannequin
Adapted from Shah (2008) and Bouchut (2011) [13, 14]

Shah's method for data collection consisted of attaching a tri-axial accelerometer to the forehead of a neonatal resuscitation mannequin. These results suggest that reasonable information may be obtained regarding the cumulative vibration experienced by the neonates' head, more explicitly, by the germinal matrix itself. However, their setup was influenced by rigid body motion which happened due to shifts in position of the mannequin's head. This effect lead to an unclear characterization of the dynamics experienced by the preterm infant; therefore, direct comparison between their results and the results presented in this document cannot be made.

Bouchut's method consisted of rigidly attaching an accelerometer to the inside corner of the transport incubator placed in both ground and aerial ambulances. The results on this study show that, while the overall accelerations and vibration levels were higher in the aerial than in the ground vehicle, the variance was higher in the ground than in the aerial vehicle. An important observation made in this study is that the rapid deceleration induced by the landing of the aircraft produces a larger magnitude acceleration that the ground vehicle which leads to a sudden increase in cerebral venous perfusion [13].

Chapter 3: Methods

3.1 Introduction

The procedures for modeling the environment experienced by neonates during both aerial and ground transports are described in detail in this chapter. To model the environment, various physical measurements, such as acceleration forces, acoustic noise, temperature, pressure and light intensity, are collected during the entire duration of the transport. No neonates were transported during the acquisition of the measurements. A portable custom design data acquisition device was implemented to make the above mentioned measurements during transport, which consists of calibrated sensors, signal conditioning circuitry, and a low voltage battery. Software was developed to make the measurements, to consolidate the measurements from the different sensors, time stamp the consolidated data, and store the resulting data into an external memory. In the case of the acoustic noise measurements, real-time digital signal processing was implemented to perform a sound spectral analysis. Measurements inside and outside the transport incubator were performed at the same time not only to characterize the environment in the transport, but also to determine the effects that the transport incubator has on premature babies during transport.

3.2 Measurements in the Transport Environment

The characterization of the environment in neonatal ground and aerial transports consists of gathering various environmental risk factors of significance which are justified by the research presented in the literature review of this document. The study conducted by Shah et al. noted that impulses induced by transport are the cause of morbidity in premature infants and adversely affecting them in two ways, by direct concussions to their underdeveloped germinal matrix and by plausible extubation [14]. The results obtained in their study present a maximum measured acceleration of 39 m/s^2. The studies conducted by Sitting et al. and Bouchut et al. show results of measured sound levels inside incubators during transports of up to 93 dB sound pressure level. In addition, Antonucci et al. found in their research that other environmental risk factors exist, such as drops in environmental temperatures that causes high levels of heat loss and bright light exposure which adversely affects the neonates' physiology [11]. As discussed in the physiological risk factors section of this document, the changes in cardiac rhythms induced by low body temperature and exposure to bright lights present an increased

probability for the development of IVH. Table 3-1 presents the measurable physical stressors that make up the proposed model of the neonatal transport environment.

Table 3-1. Summary of the suspected risk factors found in both NICU's and neonatal transports

Risk Factor	Range	Justification
Accelerations	Up to 4 G's	Maximum G-force measured in Shah et al. study [14]
Noise Level	Up to 93 dB	Maximum sound level measured in Sitting et al. study [12]
Ambient Temperature	25 ºC – 32 ºC	Suggested incubator temperature range as noted in Antonucci et al. study [11]
Ambient Pressure	50 kPa – 110 kPa	Variability in barometric pressure due to changes in elevation from 6,000 meters down to sea level [28]
Ambient Light	Up to 10,000 lux	Equivalent light exposure to a clear sunny day [29]

3.3 Data Acquisition System Design

The device used to quantify the factors of interest consists of a power circuit, an array of sensors selected based on the criteria mentioned in Table 3-1, a central processing unit, and an external memory for data storage. Software was developed to collect data, to process it in real time, and to store it onto an external memory card. The system was designed so that it could collect data from the environment for a maximum period of five hours.

3.3.1 Data Acquisition Device Hardware

The requirements for the overall monitoring system were those of a rugged, portable, and compact device. Additionally the device needed to be battery powered and capable of logging data for extended periods of time. The data acquisition device is about 10x6 centimeters (cm) in size and may be powered from either a USB source or a 3.7 Volt single cell lithium-polymer battery. The power circuit consists of two regulated step up/step down charge pumps, one that outputs 3.3 Volts and the other 5.0 Volts. A battery charge controller has been implemented which was configured to charge the battery from the USB supply and to automatically switch between USB power and battery power without interrupting any activities.

The sensor array consists of several sensors that are able to quantify different variables in the environment. A 3-axis accelerometer measured the vibration and G-forces present inside the neonatal transport incubator with a bandwidth of 160 Hz.

The x-axis measures the front to back accelerations, the y-axis measures the side to side accelerations and the z-axis measures the up and down accelerations. Figure 3-1describes the orientation of the device's accelerometer relative to the transport vehicle.

Figure 3-1. Orientation of the device's accelerometer with respect to the vehicle used for test flight

An electret condenser microphone collects acoustical noise data within the human audible bandwidth which ranges from 20 Hz up to 20 kHz. The signal from the microphone goes through a Butterworth 4th order low-pass filter and then into an analog-to-digital converter (ADC) sampling at 51.2 kHz. A thermistor, similar to those used in conventional electronic home thermostats, gathers ambient temperature. An electromechanical barometer monitors the changes in pressure inside the transport incubator that could arise from changes in elevation, especially in aerial transports. Finally, an ambient light sensor captures the ambient luminance with a wavelength of 555 nm inside the transport incubator. The specifications of the sensors selected for this device are described in Table 3-2. Appendix A contains the circuit schematics for the entire data acquisition system.

Table 3-2. Sensor array specifications of the data acquisition device

Sensor	Dynamic Range	Bandwidth	Sensitivity	Resolution
Accelerometer	-6 G's to +6 G's	160 Hz	340 LSb / G	6 mG
Microphone	106 dB (SPL)	20Hz – 20 kHz	- 44 dB / V	5.2 dB (SPL)
Thermistor	+5 ºC to +100 ºC		20 mV / ºC	0.16 ºC
Barometer	15 kPa to 115 kPa		45.9 mV / kPa	70.2 Pa
Ambient light sensor	10 lux to 10,000 lux	500 Hz	0.48 µA / Lux	1 Lux

The units that represent acceleration values are referred to as G-forces (G's) where, 1 G correspond to 9.81meters per second squared (m/s²) in metric units, which is the force experienced due to the Earth's natural gravitational pull. For simplicity, we will express vibration in m/s² and impulsive forces in G's. Acoustic data from the microphone are given in A-weighted decibel sound pressure level (dBA SPL). Temperature, pressure, and luminance are given in degrees Celsius (ºC), kilo-Pascal (kPa), and lumens per meter squared (lux), respectively. The data is collected simultaneously through an ARM-7 microcontroller which then stores the data into a Micro SD card. Figure 3-2 shows the final prototype of the data acquisition device used to characterize the environment inside neonatal transport vehicles. Appendix B contains the specification sheet for the microcontroller and for each transducer.

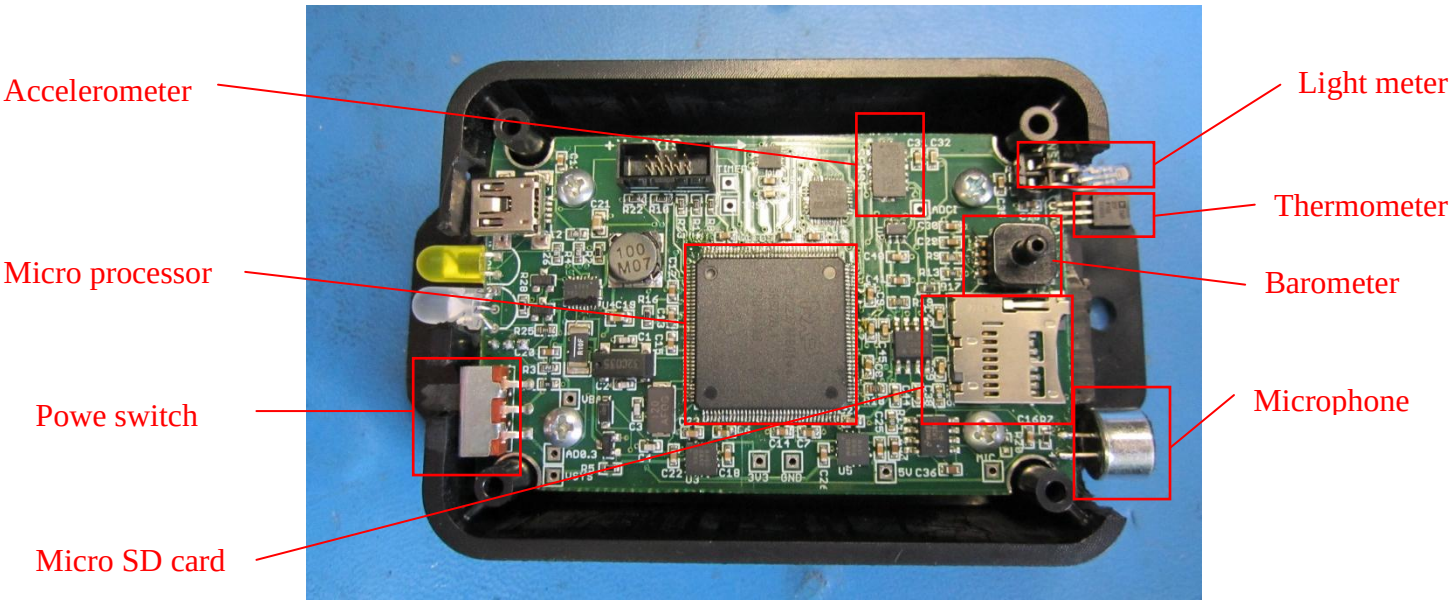

Figure 3-2. Final design of the Neonatal Intensive Care Unit – Transport Monitoring Unit (NICU-TMU)

3.3.2 Sensor Calibration and System Validation

Each sensor of the data acquisition device was calibrated by comparing the sensor data output with either a known excitation input or the output of other measuring device. The accelerometer was calibrated by comparing the output data as it was excited with a shaker table, as shown in Figure 3-3, at two specific frequencies; 40 Hz and 80Hz. No adjustments were necessary since the accelerometer was factory calibrated and responded as expected. Figure 3-4 and Figure 3-5 show the output accelerometer data for that calibration excited at 40Hz and 80Hz, respectively. The vertical axis in the plot corresponds to the magnitude and the horizontal axis to the frequency; these plots were obtained by converting the time domain data into the frequency domain by a Fast Fourier Transform (FFT). The microphone was calibrated by emitting a tone at 1 kHz and

verifying that the corresponding frequency band was excited on the acoustic spectrogram. Figure 3-6 shows the calibration setup for the microphone, which consisted of a computer playing a tone at 1 kHz, and Figure 3-6 shows the response of the microphone, which is the small yellow region in the 1 kHz center frequency. An Amprobe temperature and humidity measuring unit was used to verify that the temperature measurements from the thermometer were within reasonable values. Similarly, the measurements from the pressure and light sensor were validated by comparing their measurements with the Setra digital gauge and the Extech light meter, respectively. Figure 3-8, Figure 3-10, and Figure 3-12 show the devices used to validate the temperature, pressure, and light sensor readings, and Figure 3-8, Figure 3-10, and Figure 3-12 show the corresponding sensor outputs, respectively.

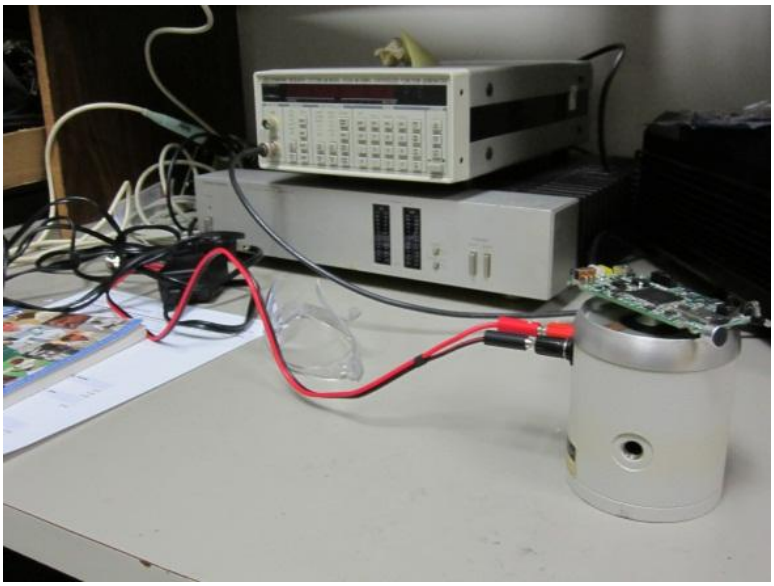

Figure 3-3. Accelerometer calibration set-up

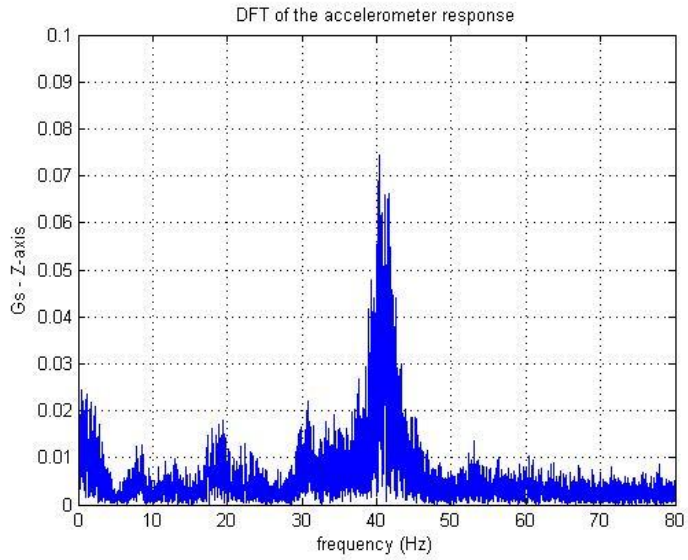

Figure 3-4. Accelerometer response excited at 40 Hz

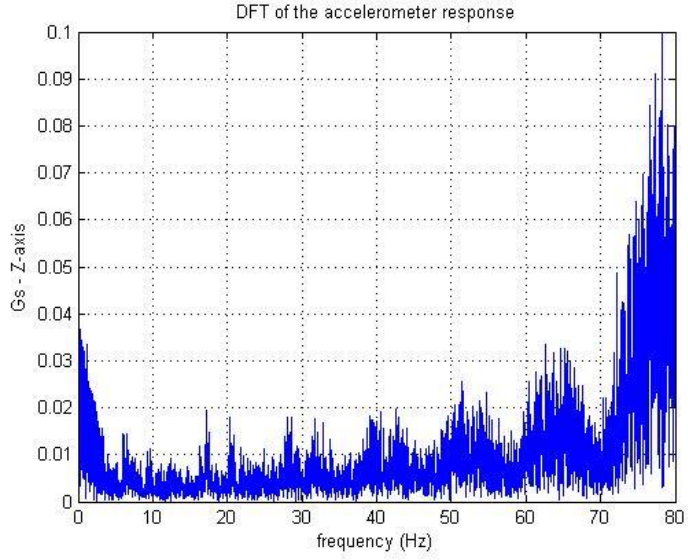

Figure 3-5. Accelerometer response excited at 80 Hz

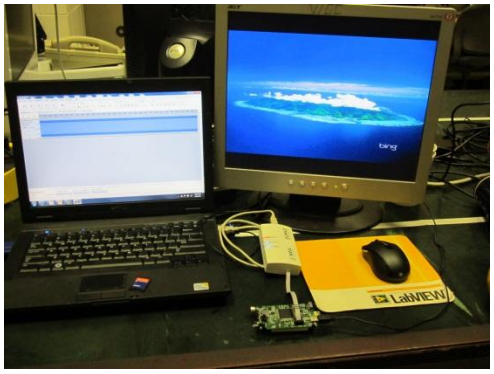

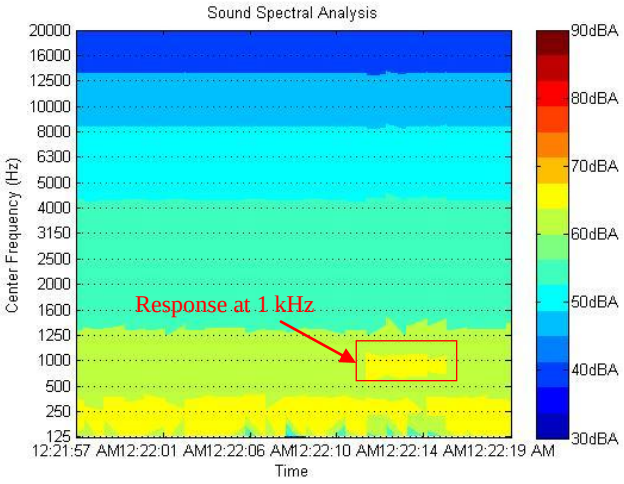

Figure 3-6. Microphone calibration set-up

Figure 3-7. Microphone response to a 1 kHz tone

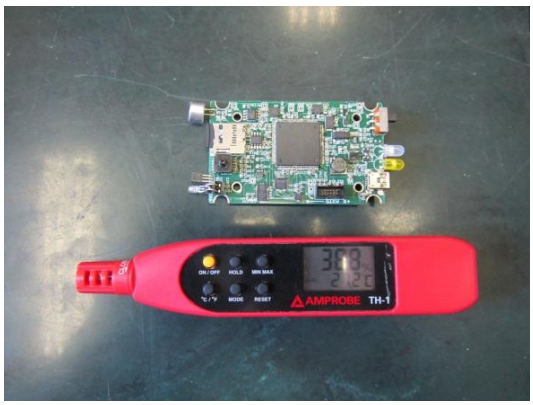

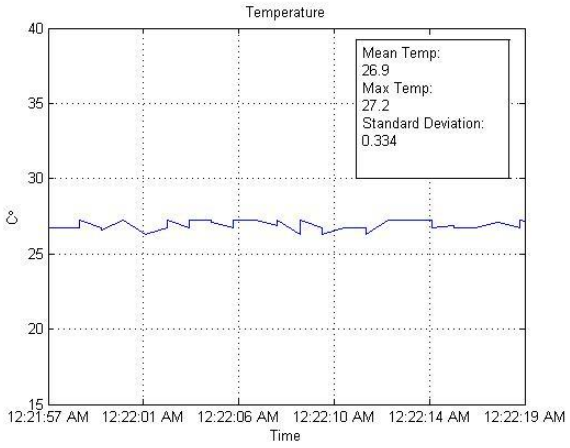

Figure 3-8. Thermistor calibration set-up

Figure 3-9. Thermistor output data

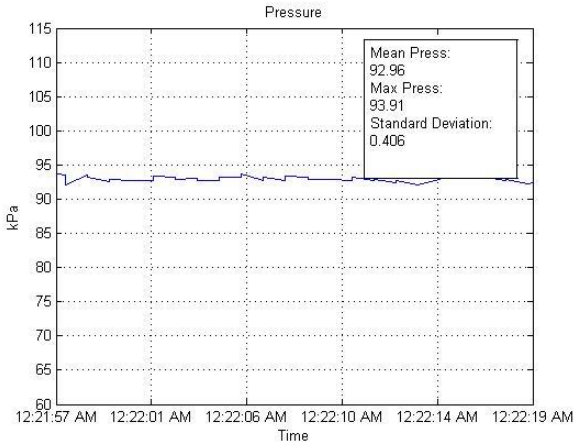

Figure 3-10. Barometer calibration set-up

Figure 3-11. Barometer output data

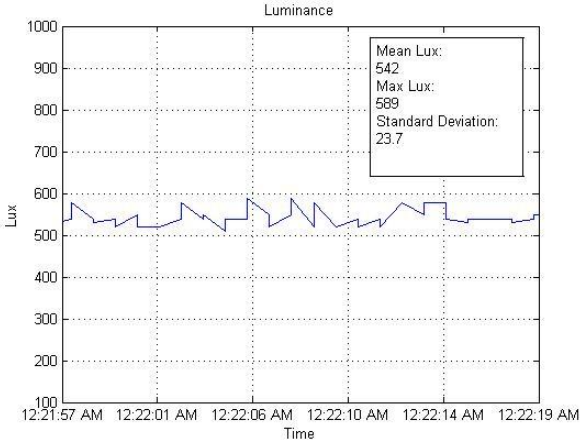

Figure 3-12. Light-meter calibration set-up

Figure 3-13, Light-light meter output data

3.4 Software Design

The software utilized for the neonatal intensive care unit transport monitoring unit (NICU-TMU) device consists of a state machine developed in a hybrid LabVIEW® and C environment. State of the art digital signal processing techniques were used to reduce the noise data into a sound spectral analysis so that the device would not be limited by its finite 2 gigabyte memory card.

The software of the NICU-TMU device was designed to be both readable and concise while effective and power conserving. The software consists of a finite state machine composed of five states which are initialize, acquire, save, sleep, and clock. A state machine is a device that changes its states based on changes of its inputs, and was chosen because of its ease to develop new software and for its simplicity which allows future

researchers to pick up on the design and make changes quickly. The architecture of the state machine implemented for this device is depicted in Figure 3-14.

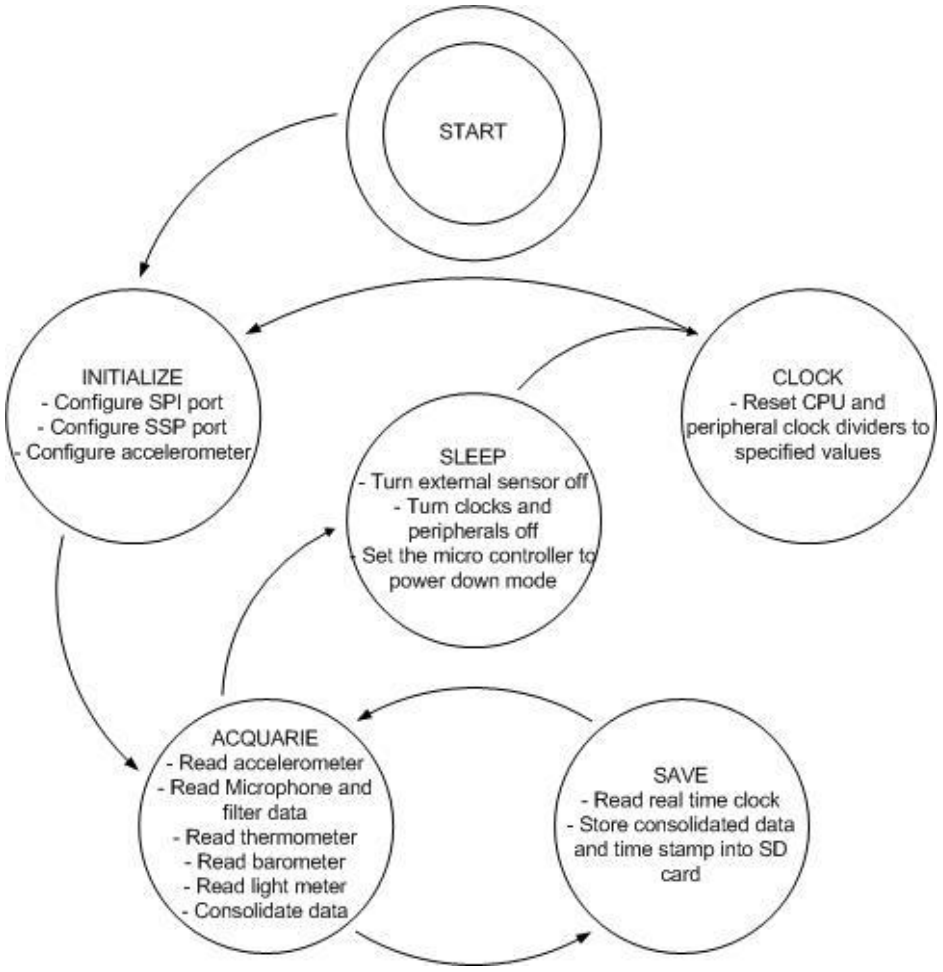

Figure 3-14. State machine diagram that describes the system's software architecture

The start of the state machine begins by simply turning the power switch to the on position. In the initialize state, software configures the serial peripheral interface (SPI) port for communication with the accelerometer, configures the synchronous serial peripheral (SSP) port for communication with the analog to digital converter which reads microphone data, and configures the accelerometer through the SPI port. Upon verifying the configuration on the accelerometer, the device switches to the acquire state, where the data from the accelerometer, thermometer, barometer, and light meter are read, and the data from the microphone is read and processed through a hybrid octaves-third octaves band pass digital filter bank into a sound spectral analysis; the data from all the sensors is finally consolidated into a string of data. Consequently the device switches to the save state where the microcontroller reads the time from the real time clock, concatenates the time stamp with the data string, and then stores the data into a micro SD card. If, within the acquire state, the readings of the accelerometer do not change significantly within a specified period of time, the device switches into the sleep state. In the sleep state,

software is used to set the wake up interrupt in the accelerometer, turn off all analog sensors, turn off and reset the microcontroller clock dividers and peripherals, and finally it turns itself into power down mode. When the accelerometer reads an absolute G-force above a preset threshold, an interrupt is triggered which wakes up the microcontroller from power down mode and resumes all activities. The clock state is entered 100 microseconds (µs) after wake up and it is responsible for setting up all of the CPU and peripheral clock dividers; An additional 500 µs are required for the Clock state. A total of 600 µs must pass before the device can begin to acquire data. These times were estimated per instruction in the microcontroller data sheet in Appendix B. Finally, the device enters the initialize state once again to reset the peripherals and the accelerometer back to acquisition mode and then the entire cycle repeats. Appendix D contains the code utilized in this monitoring unit.

3.5 Digital signal processing

The digital signal processing was broken down into two parts, real-time digital signal processing for the noise data and batch digital signal processing for the acceleration, temperature, pressure, and light data.

3.5.1 Real-time digital signal processing

Processing of the noise data in real-time was necessary since the data produced by the ADC sampling acoustic nose at 51.2 kHz was too large and would fill up the memory card in less than two hours of continuous monitoring. To alleviate this issue, a digital band pass filter bank was designed that would greatly reduce the data by performing a sound spectral analysis. A digital set of filters was preferred over an analog filter bank because digital filters have exceptional repeatability and do not require any additional power and real-estate. The filter bank consists of a hybrid octave-third octave filter bank, where the frequency bands below 1 kHz are octave bands and the frequency bands equal to and above 1 kHz are third octave bands. Table 3-3 is a summary of the specifications for each filter that make up the entire digital filter bank.

Table 3-3. Digital filter bank specifications

Center frequency (Hz)	Passband (Hz)	Filter order	Passband ripple (dB)	Stopband ripple (dB)
125	111.3 – 222.6	3	2.6	30
250	222.1 – 444.2	3	2.6	30
500	443.2 – 886.3	3	2.6	30
1000	884.2 – 1115.8	3	2.6	30
1250	1113.2 – 1404.7	3	2.6	30
1600	1401.4 – 1768.4	3	2.6	30
2000	1764.2 – 2226.3	3	2.6	30
2500	2221.1 – 2802.7	3	2.6	30
3150	2796.1 – 3528.4	3	2.6	30
4000	3520.1 – 4442.0	3	2.6	30
5000	4431.6 – 5592.2	3	2.6	30
6300	5579.0 – 7040.1	3	2.6	30
8000	7023.6 – 8863.0	3	2.6	30
10000	8842.2 – 11158.0	3	2.6	30
12500	11132.0 – 14047.0	3	2.6	30
16000	14014.0 – 17684.0	3	2.6	30
20000	17642.0 – 22263.0	3	2.6	30

Frequency bands per ANSI/ASA S1.6-1984 [30]

Two types of digital filters may be designed, the infinite impulse response (IIR) filter and the finite impulse response (FIR) filter. The IIR filter was designed for this research because this family of filters require less memory to store coefficients and is less computationally intensive than the FIR family of filters. The design begins with the set of specifications listed on Table 3-3 and, for this application, an elliptical type of bandpass filter was selected because it allows for a sharper attenuation roll off with a lower order than any other type of filter. From this selection and after computing the transfer function of the desired analog filter, the coefficients of the digital filter were calculated using the bilinear z-transform (BZT) method. In this method the poles of the selected analog filter are directly maped from the s-plane into the z-plane by relying on the Tustin approximation method. Equation (3-1 shows the Tusting approxiamtion equation

(3-1)

$$s = \frac{2}{T}\left(\frac{z-1}{z+1}\right)$$

where s is the pole in the continuous time domain, T is the sample period, which is approximately 19.5 µs, and z is the pole in the discrete time domain.

After computing the transfer function for the digital filters using the BZT method, the filter was realized using the Direct Form I (DF1) realization. Figure 3-15 illustrates the block diagram of the DF1 realization.

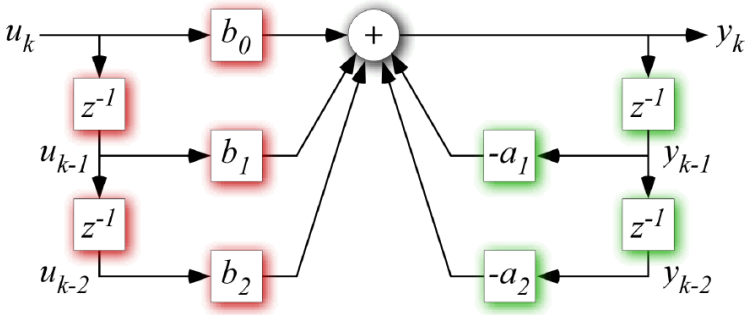

Figure 3-15. Direct Form I realization diagram

In this diagram, u_k is the input to the filter, z^{-1} is a unit time delay, b_n is the numerator coefficient, a_n is the denominator coefficient, and y_k is the output of the filter.

The most challenging part of the real-time digital signal processing was the conversion of the coefficients from floating-point, which are numbers represented in both decimals and fractions, to fixed-point, which are numbers represented in decimals only. This

conversion was necessary because this reduced the filter bank computation time by two orders of magnitude. Figure 3-16 illustrates the frequency response function of the digital octaves-third octaves filter bank which is composed of seventeen elliptical band pass filters.

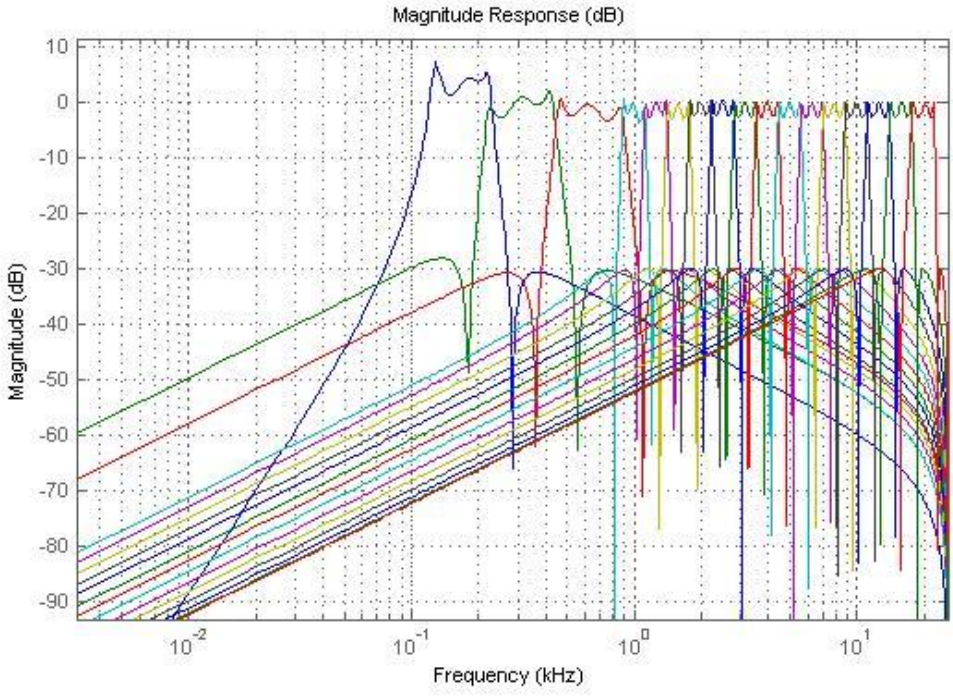

Figure 3-16. Digital filter bank frequency response function

The adverse effects of the finite word length representation are observed in the first three filters since these filters contain the smallest coefficients. In addition, filters with center frequencies below 125 Hz could not be implemented because of the limitations of the microcontroller.

The implementation of the digital filter bank consisted of computing the output equation of the diagram shown in Figure 3-15, which is given by Equation (3-2).

(3-2)

$$y_k = b_0 u_k + b_1 u_{k-1} + b_2 u_{k-2} - a_1 y_{k-1} - a_2 y_{k-2}$$

3.5.2 Batch digital signal processing

The batch digital signal processing consists of using the NICU-TMU to collect data and then store it in the raw binary form. Then, with a more capable computer, the raw data is converted into the corresponding measurement. The voltages read from the thermometer, is scaled to its corresponding measurement in °C by computing Equation (3-3).

(3-3)

$$T = \frac{T_b}{1} \cdot \frac{3.3\,V}{1024_b} \cdot \frac{°C}{0.02V}$$

where T is the temperature in °C, T_b is the raw binary input from the ADC, and 1024_b is the resolution of the ADC. Similarly, the voltages read from the pressure transducer are scaled to its corresponding measurement in kPa by computing Equation (3-4).

(3-4)

$$P = \frac{P_b}{1} \cdot \frac{3.3\,V}{1024_b} \cdot \frac{51\,k\Omega}{33\,k\Omega} \cdot \frac{1\,kPa}{0.009 \cdot 5V} \cdot \frac{0.95}{0.009}$$

where P is pressure in kPa and P_b is the raw binary input. Lastly, the readings from the light meter transducer are scaled to its corresponding measurement by computing Equation (3-5).

(3-5)

$$Lux = \frac{Lux_b}{1} \cdot \frac{3.3\,V}{1024_b} \cdot \frac{1}{681\,\Omega} \cdot \frac{10\,Lux}{0.0000048\,A}$$

Where lux is the lumens per square meter and lux_b is the raw binary input. These equations were derived from the physical measurement to voltage relationship for the temperature and pressure transducers and from the physical measurement to current relationship for the luminance transducer as specified in the data sheets in Appendix B.

For the case of the accelerometer, data is broken down into batches of 25 seconds and a vibration spectrogram was created where frequency and magnitude of the vibrations are plotted versus time on a color map. Figure 3-17 presents the calibration excitation as measured by the accelerometer over time.

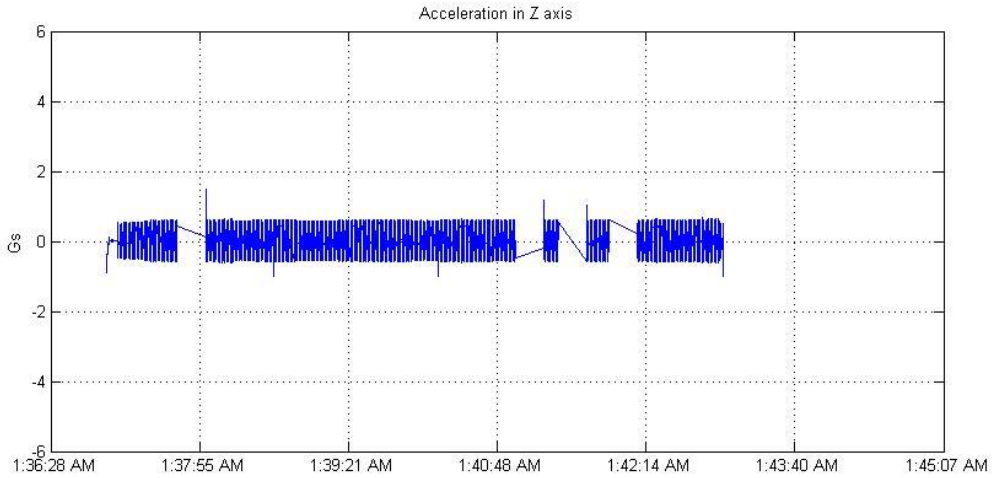

Figure 3-17. Acceleration vs. time plot measured in G's

By taking the short time Fast Fourier Transforms (SFFT) and plotting them on a color map, a vibration spectrogram may be computed as shown in Figure 3-18.

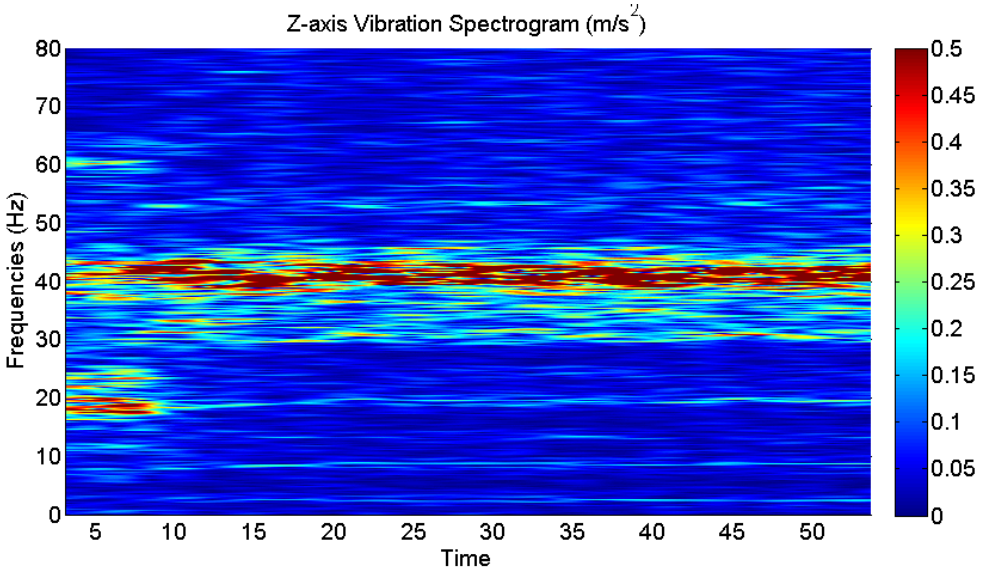

Figure 3-18. Vibration spectrogram measured in m/s² at a given frequency over time

The size of the SFFT's for this research was 1024 samples with 1019 samples of overlap. A Hamming window was implemented on every SFFT block.

3.6 Approach

Two NICU-TMU devices are utilized during either aerial or ground transport. One located within the transport incubator where the neonates' head is positioned, and the

other outside of the transport incubator attached to any surface of the interior of the vehicle with the positive x-axis of the accelerometer pointing towards the back of the vehicle for both devices as shown in the example in Figure 3-19.

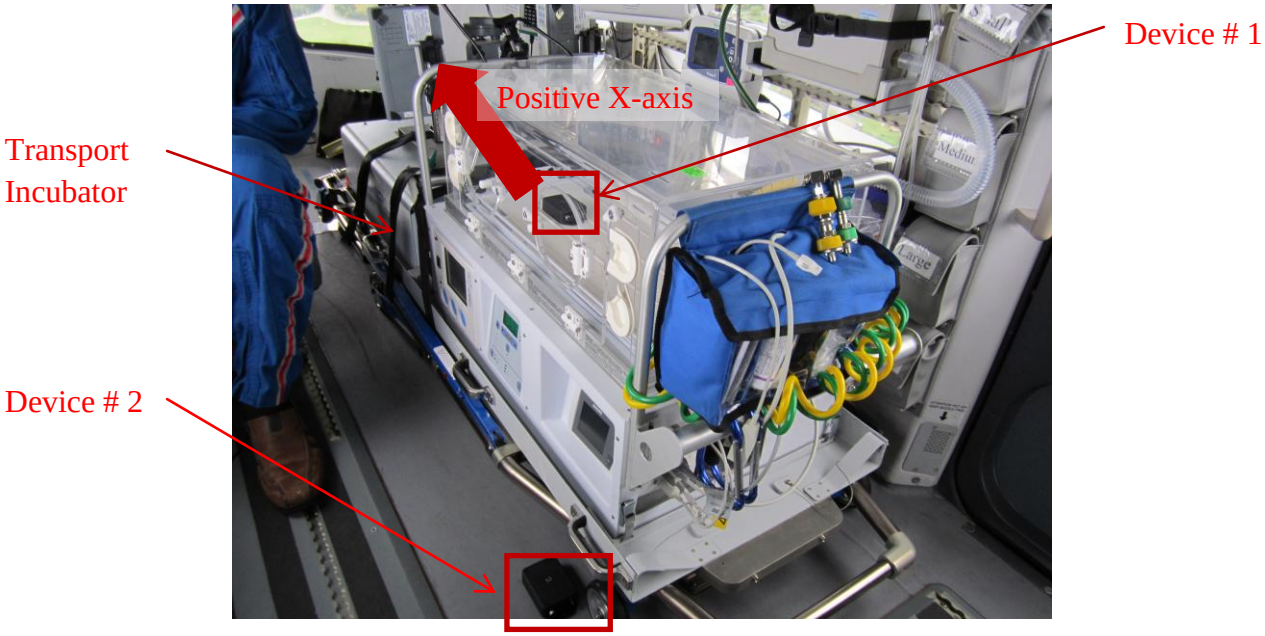

Figure 3-19. NICU-TMU setup

No neonates are to be transported while measurements are being made. Vibration spectrograms were created to identify the vibrations and their corresponding frequencies present during transport. Additionally, histograms were created to discover the occurrence of high magnitude impulses that cannot be identified in the spectrogram. The goal of this approach is to determine what the role of the transport incubator is in to determine whether it is attenuating or amplifying the physical stressors induced by the vehicle. All this was done in an effort to justify the need for the development of a new state of the art transport incubator that will mitigate the IVH problem.

Chapter 4: Results and Discussion

4.1 Introduction

The measurements collected during both a 4 hour car ride and a 30 minute helicopter flight are presented in this chapter. The data for a 4 hour road trip is presented to give the reader an idea of the stressors present during a typical road trip. The test flight departed at 10:44 am from the Carilion Clinic Patient Transport (CCPT) hangar and consisted of flying out to the Roanoke Airport, out to Pulaski, and then back to the CCPT hangar. Average speed was 110 knots with a maximum speed of 135 knots at 11:20 am. There were only one take-off and one landing event for the helicopter experiment. Measurements were made both inside and outside the transport incubator during transport. Vibration spectrograms, sound spectrograms, as well as the changes in temperature, pressure, and luminance were computed using the techniques explained in chapter 3. A description of the environments inside and outside the incubator inside the vehicle is presented and the differences are discussed. Finally, the effects of the physical stressors in both adults and premature babies are discussed.

4.2 Monitoring a Passenger Car Environment

The data presented in this section was taken during a test drive from Washington, District of Columbia to Blacksburg, Virginia. The purpose of this experiment was to verify the validity of the measurements and to generate a base model to compare to the environment in the neonatal transport environment. Figure 4-1 shows the acceleration forces over time present during test drive.

4.2.1 Acceleration forces present during test drive

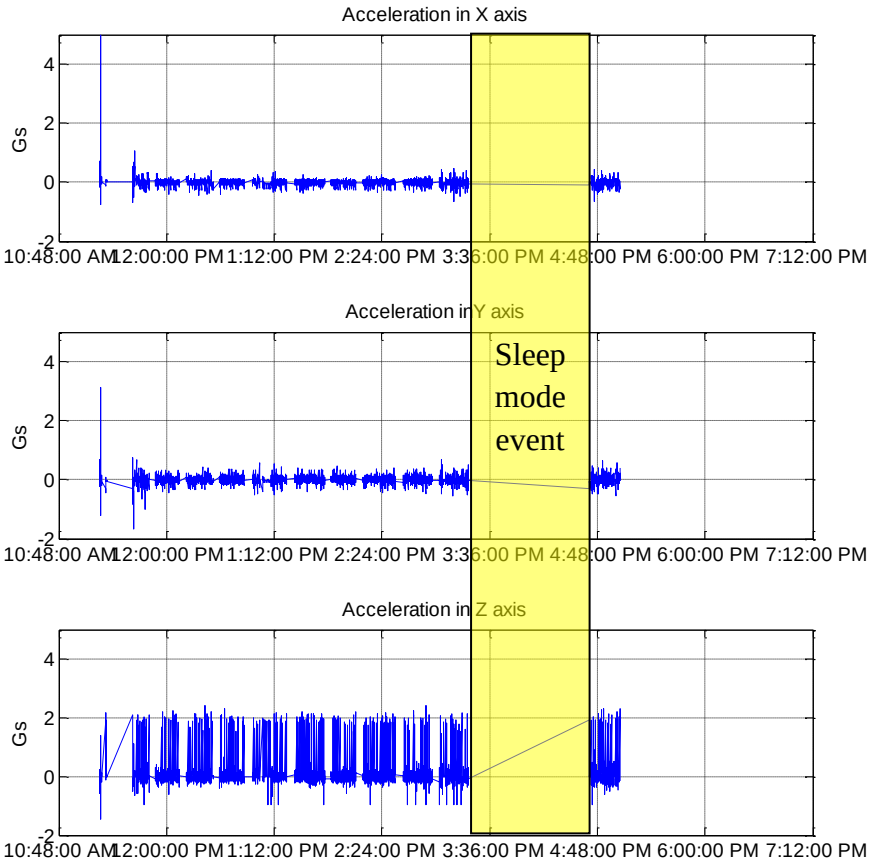

Figure 4-1. Acceleration forces versus time for all three axes of the accelerometer during test drive

Spaces or gaps between vibration measurements represent periods of missing data. This was due to the device switching into sleep mode, which was due to the threshold of inactivity being set too high. This was fined tuned after these undesired sleep events were observed. This is the form in which the data is obtained from the accelerometer. From this data, it is possible to extract vibration information and its corresponding frequencies.

Vibration spectrograms were computed to present the level of vibration in the test vehicle. These spectrograms were created by taking a short FFT of the accelerometer data and plotting it on a color map versus time. The magnitude of the vibration is given by the different colors and is expressed in m/s^2. Figure 4-2 presents the vibration present along the X-axis during test drive.

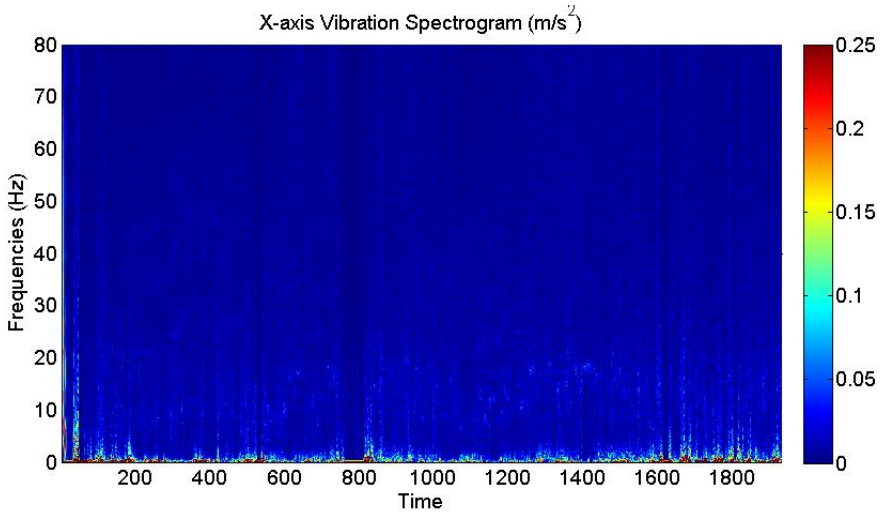

Figure 4-2. Vibrations present along the X-axis during test drive

The spectrogram suggests that the vibration level was low with values up to around 0.1 m/s² at frequencies below 5 Hz. These low frequencies were most likely due to decelerations and acceleration events. Figure 4-3 presents the vibration present along the Y-axis during test drive.

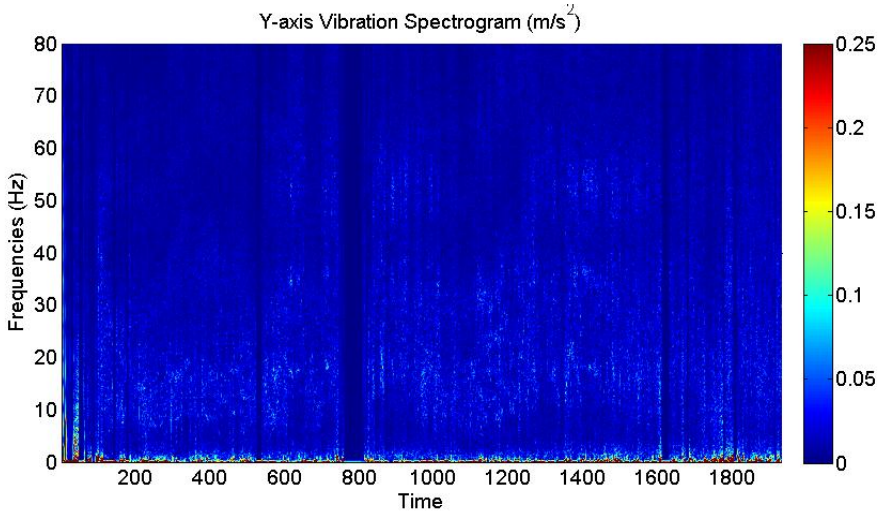

Figure 4-3. Vibrations present along the Y-axis during test drive

There was little or no vibration present in this direction. The spectrogram suggests that most of the acceleration forces occurred below 5 Hz. These values were most likely due to steering. Figure 4-4 presents the vibration levels along the Z-axis during transport.

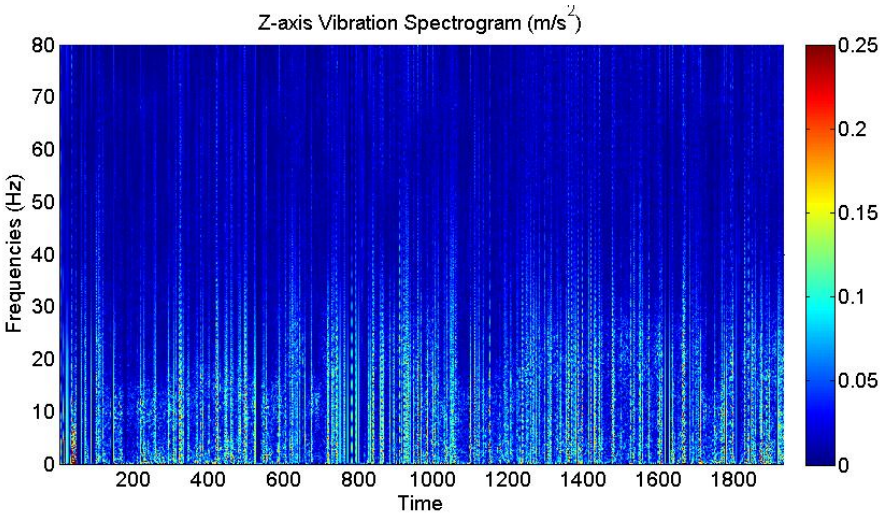

Figure 4-4. Vibrations present along the Z-axis during test drive

Significantly more vibration was present in this direction. Vibration reached up to around 0.1 m/s² with frequencies up to 25 Hz. Most of this vibration may have been induced by the different conditions of the road and the occasional impact between the board and the dash of the vehicle.

4.2.2 Noise levels and corresponding pitch present during test drive

Figure 4-5 is a spectrogram that presents the noise data during test drive. The vertical axis corresponds to the frequency or pitch of the sound, the horizontal axis corresponds to time, and the different color intensities correspond to the magnitude or loudness of the sound.

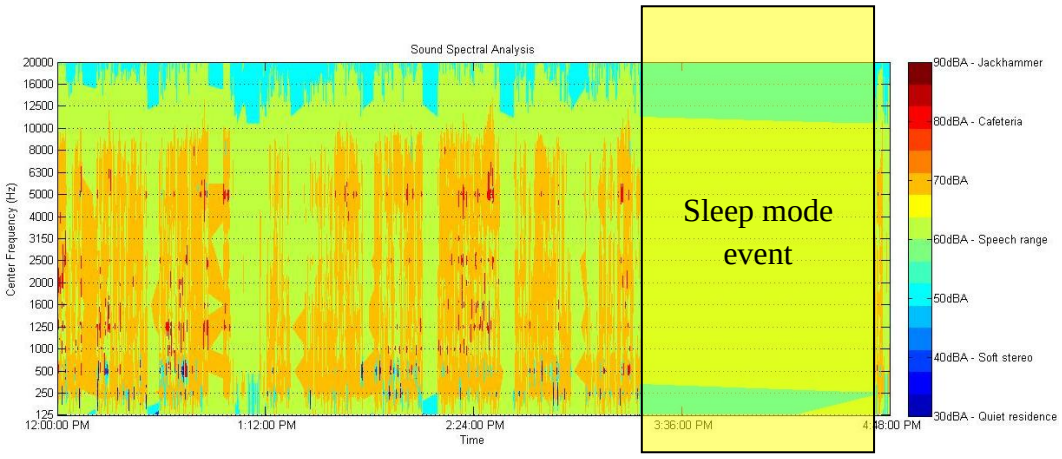

Figure 4-5. Sound spectrogram of the noise present during test drive

Results show the sound levels and the corresponding frequencies during a typical car ride. Sound levels equal to and above 70 dBA were produced by the entertainment system in the vehicle.

4.2.3 Variation of ambient temperature and pressure during test drive

This section contains the temperature and pressure measurements during test drive. Luminance measurements were not recorded for this test ride. Figure 4-6 presents the changes in temperature during test drive.

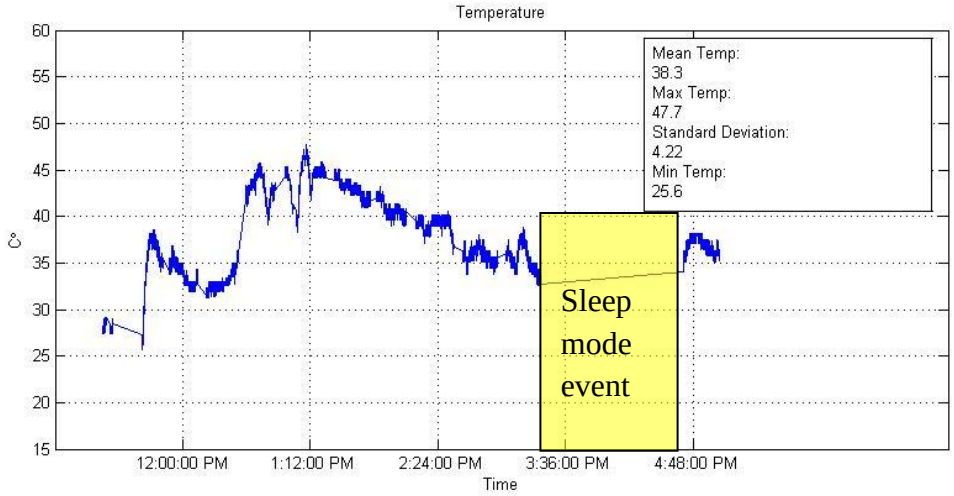

Figure 4-6. Temperature variation over time during test drive

The temperature changes in this experiment show when the device was transported from the place of origin into a hot car. Then, temperature started to decline because of the air conditioning system. The sudden spike occurred when the device was under direct sunlight.

Figure 4-7 presents the pressure changes over time during test drive. Results show that pressure declined over time. As expected, the pressure dropped as the vehicle was moving into a higher elevation.

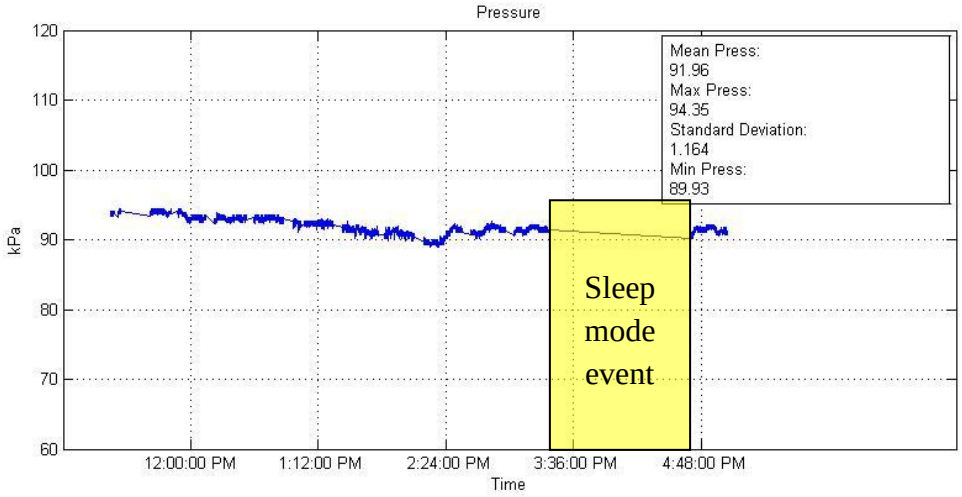

Figure 4-7. Pressure variation over time during test drive

The yellow block indicates that the device went into sleep for a long period of time. This even occurred at the moment when the driver took a break in between the road trip.

4.3 Monitoring the Vehicle Environment

The crew cabin experimental model consisted of making measurements inside the vehicle during transport. The data acquisition device was attached to the floor of the vehicle and data was collected during the entire flight. The measurements are presented in the following subsections.

4.3.1 Acceleration forces present in the vehicle environment

Figure 4-8 presents the acceleration forces over time for the tri-axial accelerometer used in this experiment. The figure consists of the acceleration forces versus time in the X, Y, and Z axes.

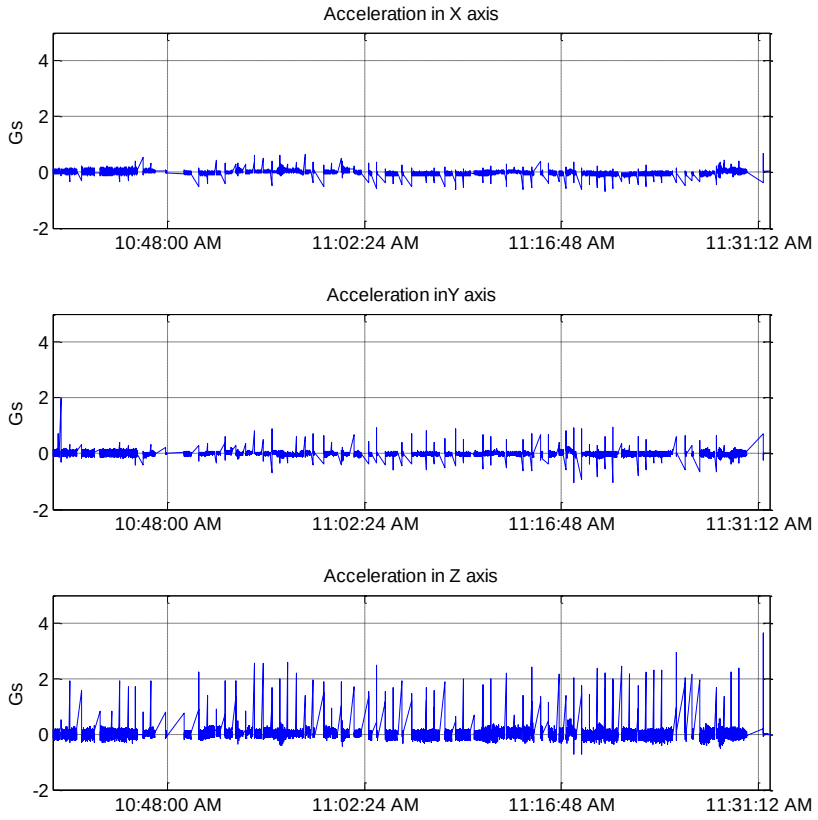

Figure 4-8. Acceleration forces versus time for all three axes of the accelerometer during transport

Although the inactivity threshold was reduced, the threshold was still higher that was required, which lead undesired sleep events. To extract the vibration information from this data, an FFT was performed on one 1024 samples long portion of the data. Figure 4-9 shows the resulting FFT plot.

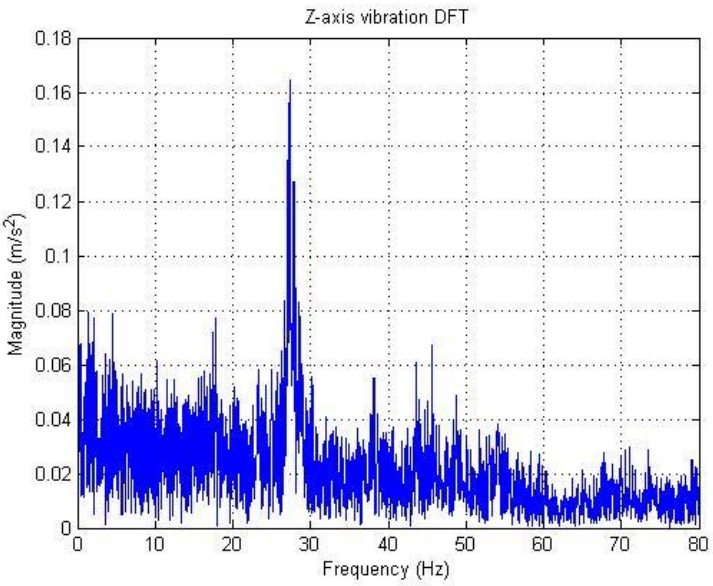

Figure 4-9. Single FFT plot of the vibration in the up and down direction

Multiple FFT's were computed for the rest of the data with blocks of 1024 samples with 1019 samples of overlap. A Hamming window was applied to each block of data. Plotting multiple FFT's over a period of time results in a spectrogram that presents the level of vibration in the cabin of the helicopter. Figure 4-10 shows the vibration present along the X-axis.

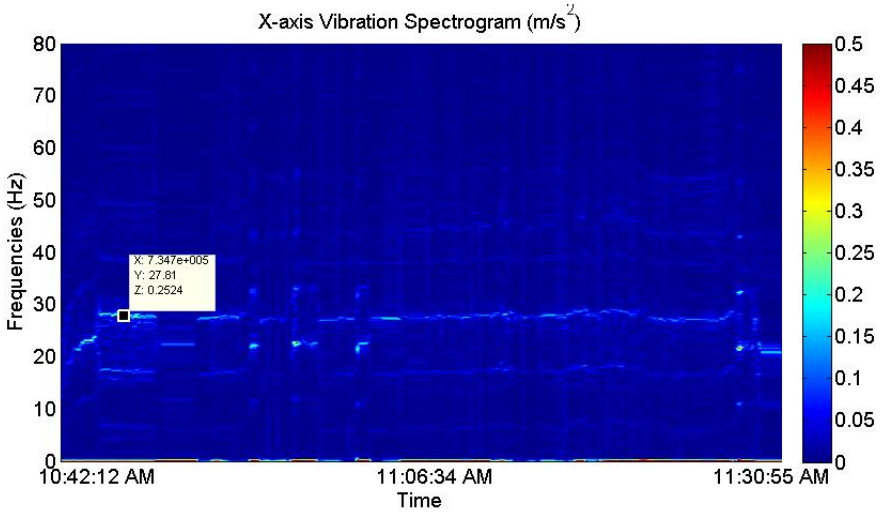

Figure 4-10. Vibrations present along the X-axis during transport

The maximum vibration sensed by the accelerometer in this direction was around 0.25 m/s² at a frequency of 27 Hz which occurred shortly after takeoff. Figure 4-11 presents the vibration present along the Y-axis.

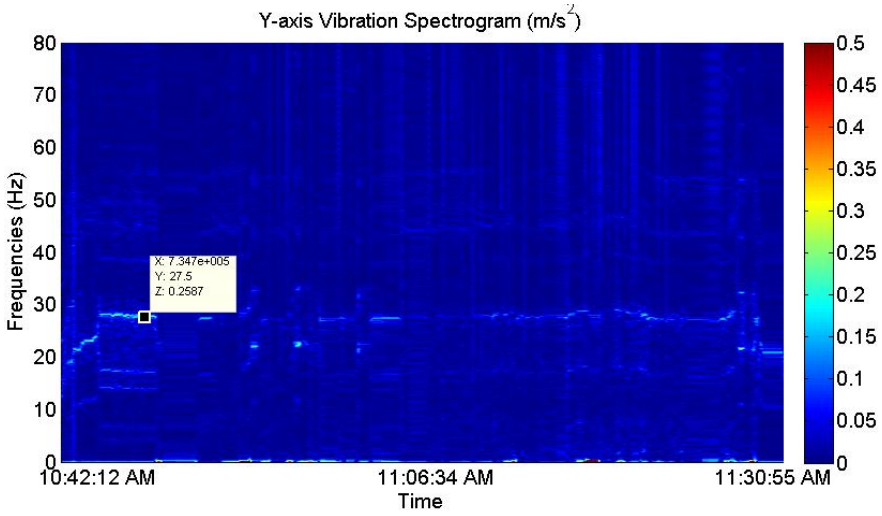

Figure 4-11. Vibrations present along the Y-axis during transport

Similar to Figure 4-10, the highest magnitude was around 0.25 m/s² at a frequency of 27 Hz soon after takeoff. Figure 4-12 present the vibration along the Z-axis.

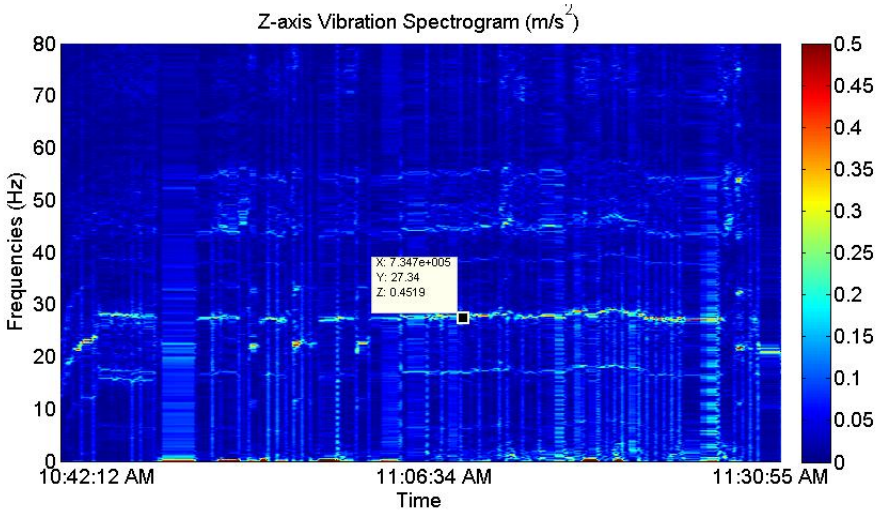

Figure 4-12. Vibrations present along the Z-axis during transport

In contrast to what was recorded by the X and Y axes of the accelerometer, the vibration along the Z-axis remained higher during the duration of the flight. Average vibration was around 0.2 m/s² with peak values up to 0.48=5 m/s². The frequency of vibration also changed with elevation, with the lower values occurring during takeoff and landing. The vibration shown in the above mentioned figures was recorded in the cabin, outside of the transport incubator.

4.3.2 Noise levels and corresponding pitch present in the vehicle environment

Figure 4-13 presents the sound data in a sound spectral analysis plot that define the tones and their magnitude present in the environment.

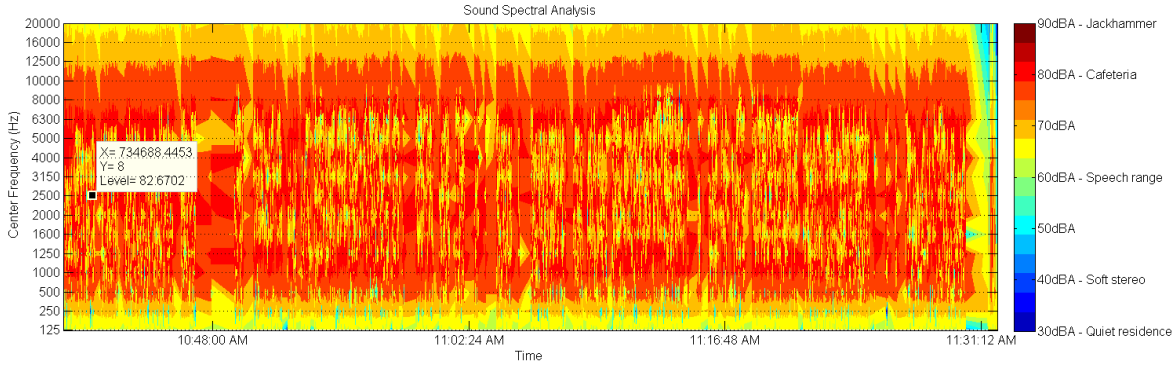

Figure 4-13. Sound spectrogram of the noise present during transport

Average sound levels up to 80 dBA were registered in the cabin with frequencies between 500 Hz and 12,500 Hz a maximum level of 82 dBA was registered at a frequency of 2.5 kHz.

4.3.3 Variation of ambient temperature pressure and light in the transport environment

This section contains the temperature pressure and luminance versus time plots that describe the change of these variables over time; also, the mean, maximum, and variance of each measurement that define the dynamics of such measurements. Figure 4-14 presents the temperature changes during the flight.

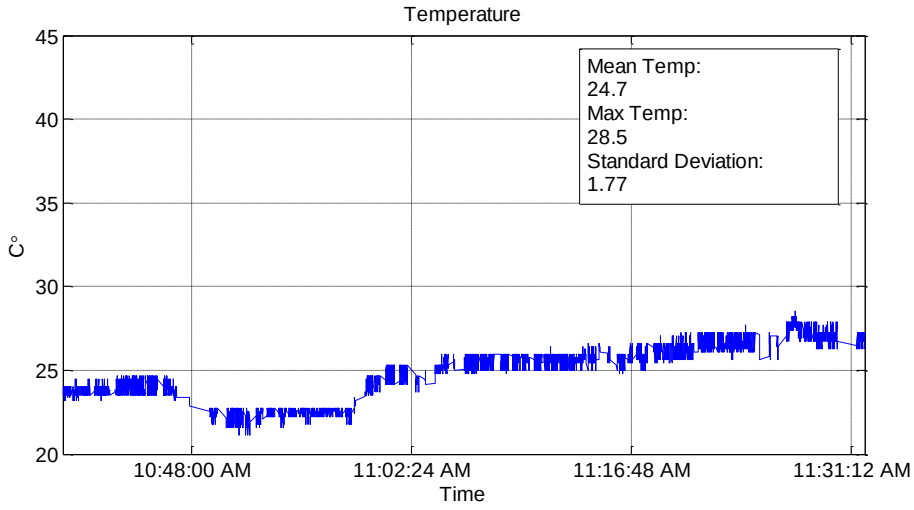

Figure 4-14. Temperature variation over time during transport

The mean temperature was 24.7 °C with a small variation of ±3.13 °C. Figure 4-15 presents the absolute pressure measurements and corresponding changes during flight.

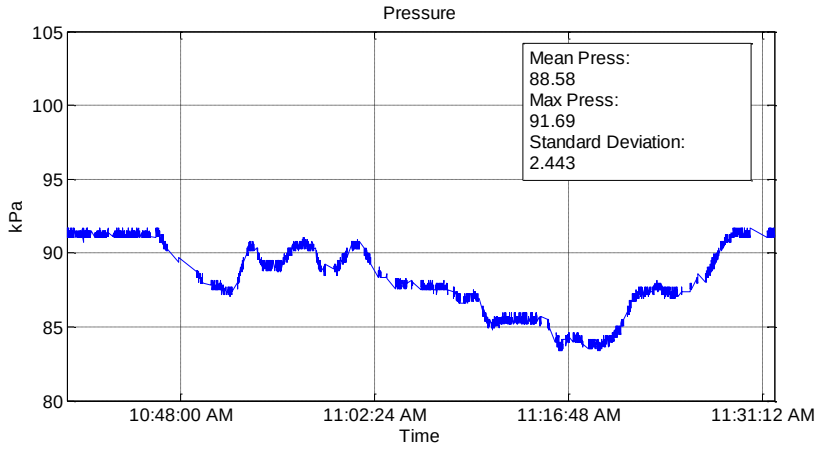

Figure 4-15. Pressure variation over time during transport

Mean absolute pressure was 88.6 kPa with a variance of ±5.97 kPa. Figure 4-16 present the changes in ambient light during flight.

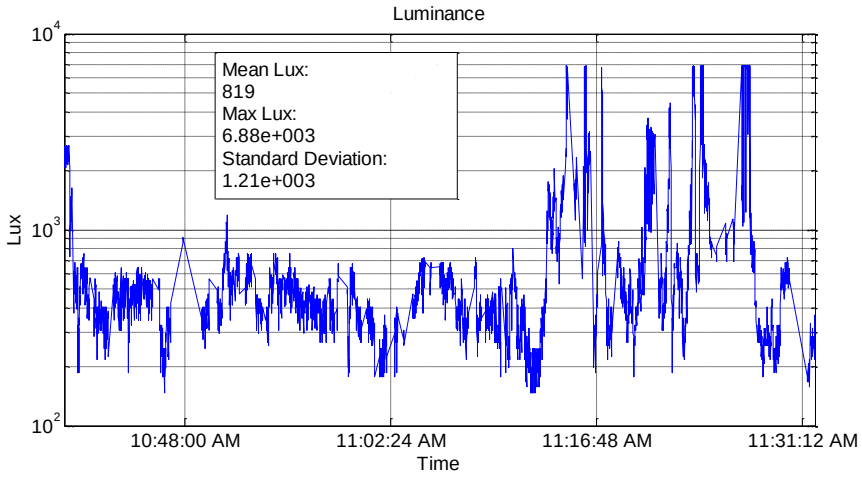

Figure 4-16. Luminance variation over time during transport

The mean recorder luminance was 819 lux with a maximum luminance value of 6,880 lux. The luminance value equivalent to direct sun light exposure is 10,000 lux.

4.4 Monitoring the Transport Incubator Environment

The transport incubator experimental model consisted of making measurements inside the transport incubator during transport. The data acquisition device was attached to the area where the baby's head rests and data was collected during the entire flight. All padding

was removed from the incubator during this experiment. The measurements are presented in the following subsections.

4.4.1 Acceleration forces present in the incubator environment

This section presents the same results as the previous section but with the measurements being taken inside the incubator where the baby's head is positioned. Figure 4-17 presents the acceleration forces over time present in the transport incubator.

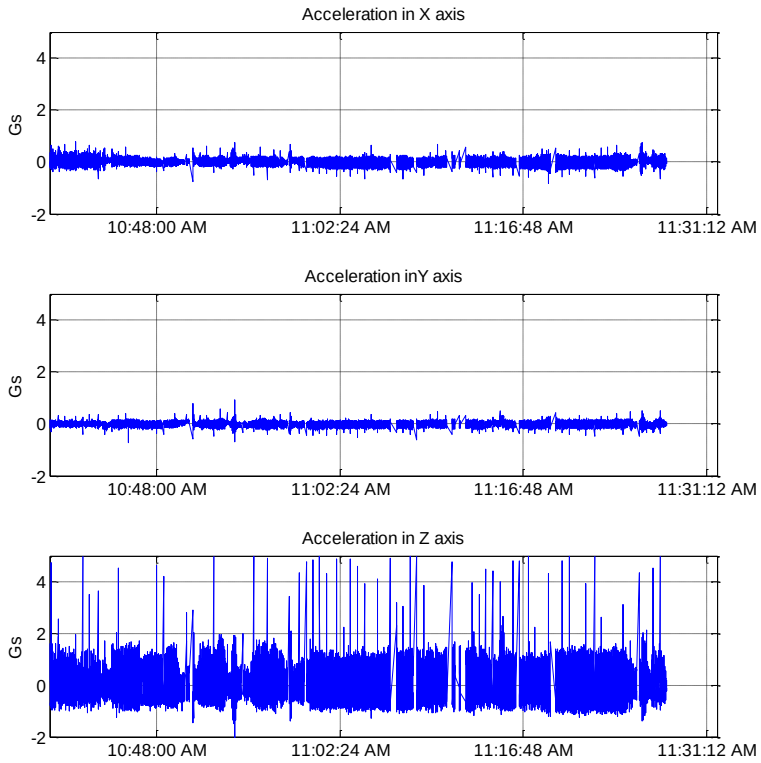

Figure 4-17. Acceleration forces versus time for all three axes of the accelerometer during transport

It can be observed that undesired sleep events did not occur inside the incubator, because the vibration was much higher than the inactivity threshold. As done in the previous section, a block of data was chosen in the up and down direction and the FFT shown in Figure 4-18 was computed.

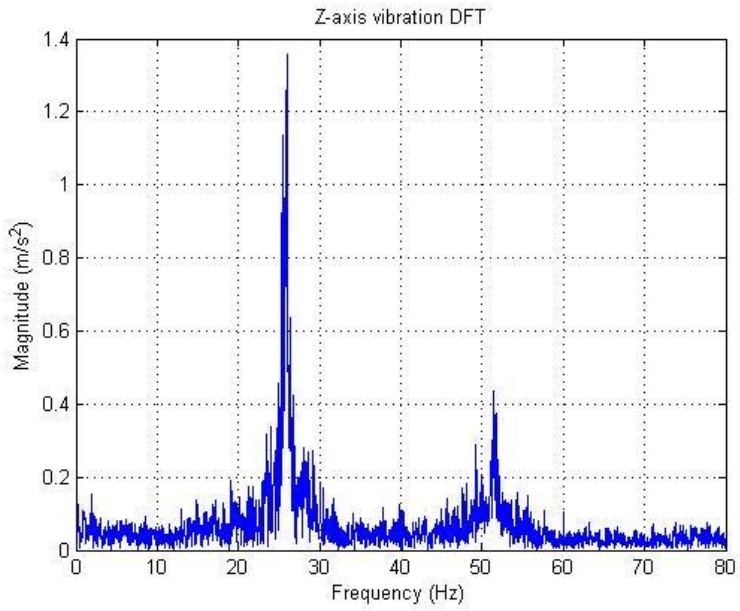

Figure 4-18. Single FFT plot of the vibration in the up and down direction

Results of the FFT show that there were significant levels of vibration at 25 Hz with a harmonic response at around 50 Hz.

Figure 4-19 shows a spectrogram analysis plot that presents the vibration in the environment.

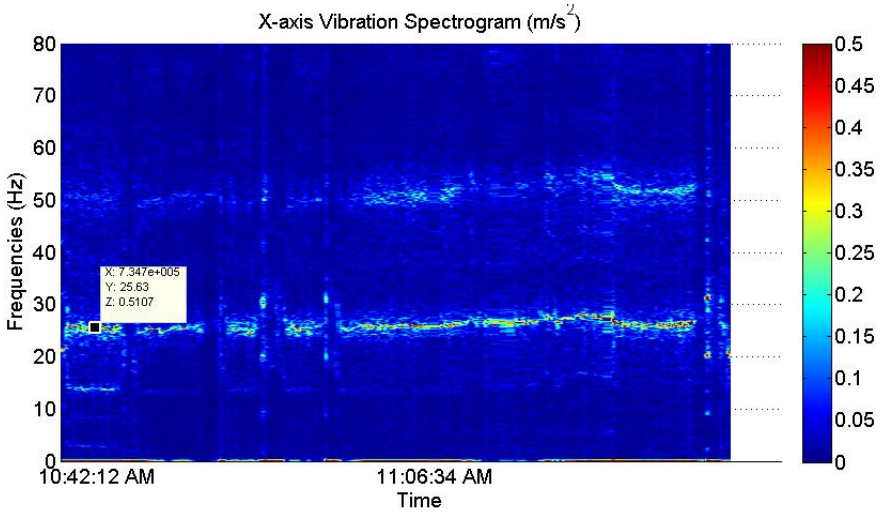

Figure 4-19. Vibrations present along the X-axis during transport

The spectrogram shows that vibrations were present along the X-axis. An average vibration of 0.2 m/s² at around 25 Hz was recorded with a harmonic at around 50 Hz a maximum vibration of 0.51 m/s² at a frequency of 25 Hz was registered. Figure 4-20 presents the vibration along the Y-axis.

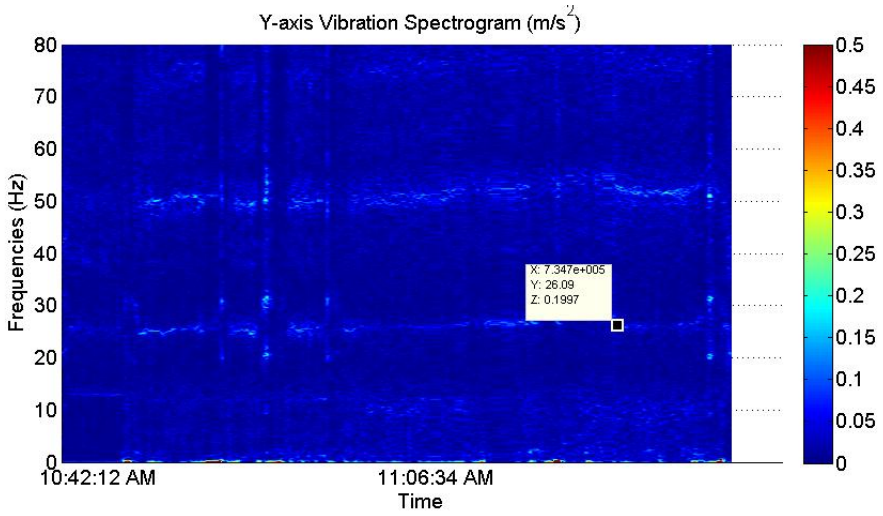

Figure 4-20. Vibrations present along the Y-axis during transport

Interestingly enough, the average magnitude of the vibration was just over 0.05 m/s² in this direction. Figure 4-21 presents the vibration along the Z-axis during flight.

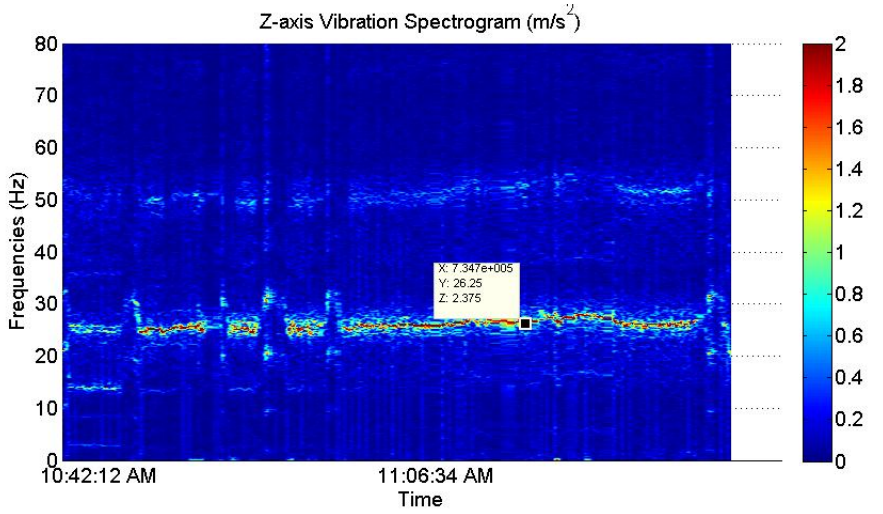

Figure 4-21. Vibrations present along the Z-axis during transport

The average magnitude of vibration was around 0.8 m/s² at around 26 Hz. It was observed that there were periods of time where the vibration levels exceeded 2 m/s². These measurements agree with what was recorded in the study made by Bouchut [13].

4.4.2 Noise levels and their corresponding pitch present in the incubator environment

To correspond to the measurements taken in the cabin, Figure 4-22 presents the sound spectral analysis plot that define the tones and their magnitude present in the incubator environment.

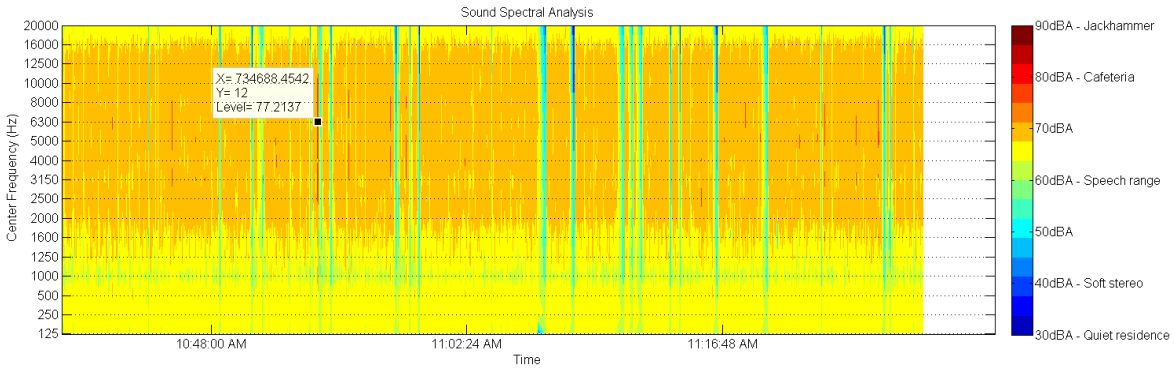

Figure 4-22. Sound spectrogram of the noise present during transport

Sound levels registered in the incubator averaged just over 70 dBA with frequencies ranging from 1.6 kHz to 16 kHz with a maximum level of 77 dBA at 6.3 kHz. These results suggest that the incubator is attenuating some noise with higher attenuations occurring at frequencies below 1.25 kHz.

4.4.3 Variation of ambient temperature pressure and light in the incubator environment

The changes in temperature pressure and luminance recorded inside the incubator during flight are presented in this section. Figure 4-23 presents the changes in temperature inside the incubator during transport.

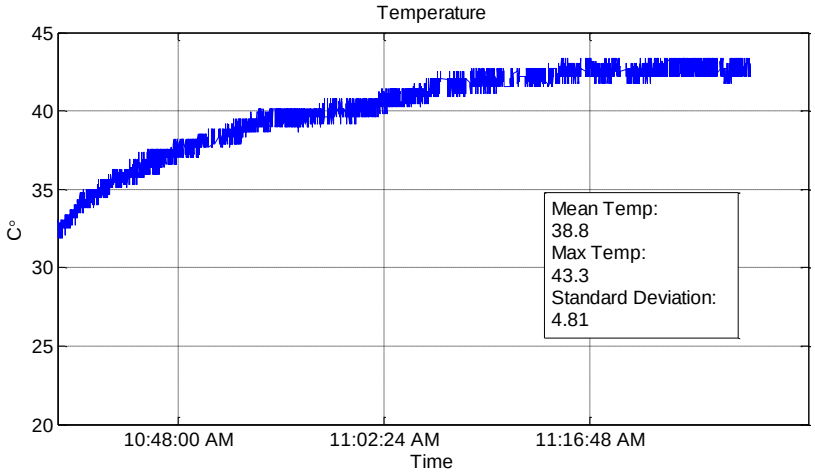

Figure 4-23. Temperature variation over time in incubator during transport

Results suggest that the temperature control in the transport incubator did a good job at heating up the inside of the incubator. Note that the constant increase in temperature is due to the temperature controller not being able to read any feedback from the temperature probe which is usually attached to the abdomen of the premature babies. Figure 4-24 presents the pressure changes in the transport incubator.

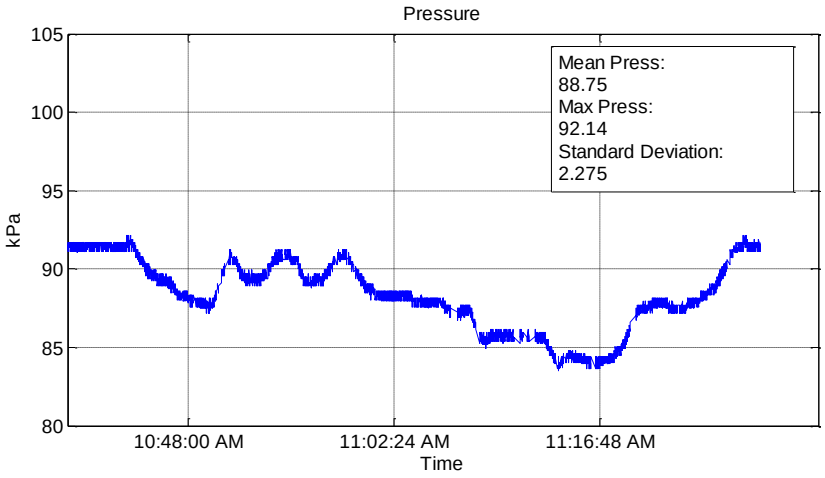

Figure 4-24. Pressure variation over time during transport

The pressure changes in the incubator correlate to those measure in the crew cabin. These results were expected since the incubator is not pressurized. Figure 4-25 presents the changes in luminance inside the transport incubator.

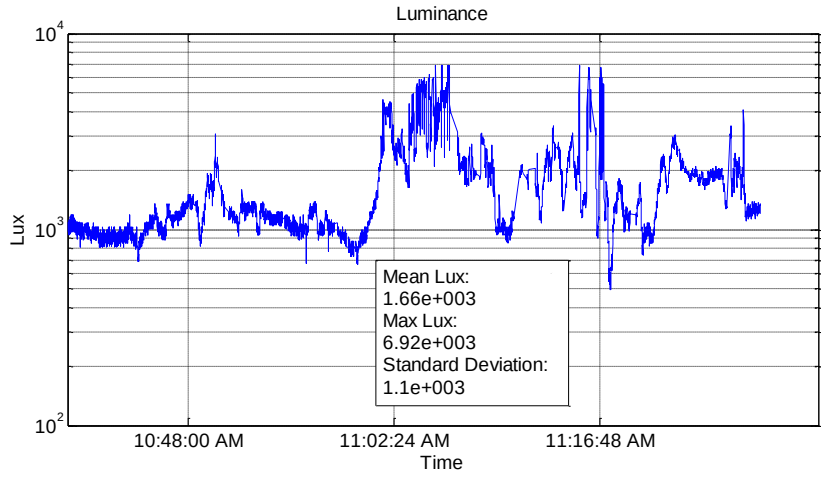

Figure 4-25. Luminance variation over time during transport

The light meter registered maximum luminance values up to 6,920 lux, evidence that inside of the transport incubator is exposed to high intensity luminance from the sun. The sensor sensitivity is similar to that of the human eye. Infrared and Ultraviolet wavelength were not measured during this experiment

4.5 Differences in the Measurements Between the Two Environments

A summary of maxima of the primary physical stressors present during transport in both inside and outside the transport incubator are presented in Table 4-1. The results show that the vibrations along the Z-axis are over two times larger, and the vibrations along the Z-axis are five times larger in the incubator. In contrast, the vibrations in the side to side direction are nearly half the magnitude inside the incubator. Overall noise levels were 5 dBA lower in the incubator than in the cabin.

Table 4-1. Summary of the maximum magnitude of the primary physical stressors during transport

	Crew Cabin		Transport Incubator	
	Magnitude	Frequency	Magnitude	Frequency
X-axis vibration	0.25 m/s²	27 Hz	0.51 m/s²	25 Hz
Y-axis vibration	0.25 m/s²	27 Hz	0.19 m/s²	26 Hz
Z-axis vibration	0.45 m/s²	27 Hz	2.3 m/s²	26 Hz
Noise levels	82 dBA	2.2 kHz - 2.8 kHz	77 dBA	5.5 kHz - 7.0 kHz

Additionally, a summary of the averages, maxima, and standard deviations of the secondary physical stressors is presented in Table 4-2. The discrepancy between crew cabin temperature and incubator temperature was due to the missing feedback from the temperature probe to the temperature controller; causing the controller to keep increasing the temperature inside the incubator. No major differences in pressure and luminance were registered between the two environments.

Table 4-2. Summary of secondary physical stressors during transport in both the crew and incubator

	Crew Cabin			Transport Incubator		
	Mean	Max	Standard Dev.	Mean	Max	Standard Dev.
Temperature	24.7	28.5	1.77	38.8	43.3	4.81
Pressure	88.5	91.6	2.44	88.7	92.1	2.27
Luminance	819	6880	1210	1660	6920	1100

Based on these results it was discovered that the combination of the current transport incubator design and the way in which it is secured to the transport vehicle amplifies the vibration. Although the current incubator design helps attenuate some of the noise, the levels registered inside the incubator are still well above 70 dBA. Continuous noise above 70 dBA has been shown to increase the risk for developing IVH in premature babies [25]. The luminance recorded during this experiment is equivalent to direct exposure to a slightly overcast sky. This suggest that the inside of the incubator does not offer protection from light exposure, and this can adversely affect a patient who is not yet ready to these kind of exposures [11]. The luminance measured in the environment was in the 555 nm wavelength. Ultraviolet and infrared were not measured for this experiment.

It is suspected that the combination of increased vibration, as well as noise over 70 dBA and high intensity light exposure significantly increase the risk for developing IVH. A change in the design of the current transport incubator that would help alleviate these stressors could tremendously decrease the risk for mortality and morbidity.

4.6 Effects of Physical Stressors

In adults the effects of acceleration forces up to 5 G's increase the cardiac demands, and acceleration forces in excess of 5 G's produce unconsciousness [14]. Loud noises in adults cause discomfort, and increased heart rate [31]. Very loud sound pressure levels may result in traumatic brain injury by direct propagation through the thoracic cavity [15]. Flickering lights flashing at about 18 flashes per second have a minimal chance of causing seizures in adults [32].

In premature babies the combination of loud noises, drops in ambient temperature and the exposure to bright lights may increase the risk for IVH. Karam et al. reported average sound levels of 88.6 dB inside incubators while operating the nCPAP driver [33]. The environmental protection agency (EPA) has suggested an average sound level of 45 dB in hospitals; therefore, continuously exposing premature infants to 88.6 dB does not only increase the risk for IVH but can also be detrimental to their hearing development [27, 33]. Changes in temperature and luminance, indirectly increase the risk for IVH by disrupting the neonates physiology [11]. Additionally, the exposure to high intensity luminance adversely affects the neonates' comfort [11].

Chapter 5: Conclusions and Future Work

5.1 Introduction

This final chapter reviews the incidence of IVH in premature babies during transport and describes the transport incubator environment briefly. The number of babies that could be saved from developing IVH and the suggestions for making improvements to the transport incubator are also described. The closing section is the summary of this document which puts emphasis in the number of premature babies born in the United States, their risk for developing IVH during transport, a hypothesis of what causes IVH, and suggestions to mitigate the IVH problem.

5.2 Suggestions for improving the quality of transport

This research has demonstrated that the environment that the preterm infant is exposed to during transport is detrimental to their health. The vibration levels registered in the transport incubator during flight were five times greater than in the crew cabin along the Z-axis. Also, high levels along the X-axis were registered in the transport incubator, which were not registered in the crew cabin. This additional vibration may be due to the back and forth motion the incubator experiences during transport as it is not rigidly attached to the helicopter. In contrast, vibration along the Y-axis was nearly half of that registered in the crew cabin. Sound levels were on average 70 dBA, which is 10 dBA lower than the crew cabin; however, the levels are still well above the recommended 45 dB sound level. Luminance levels reached values up to 6920 lux in the 555nm wavelength which are well above what unborn babies are exposed to. No major changes in temperature and pressure were registered.

IVH is a serious disease which occurs in roughly 40% of all premature babies. Although this incidence has decrease over the past three decades, the risk for developing IVH in preterm babies who require transport has not dropped from 33% within the same time frame. If this incidence during transport can be greatly mitigated, an average of 371 IVH cases could be prevented in a 3 year period. These cases were calculated assuming that 1125 children require transport in a 3 year period [7].

5.3 Future work

The results presented in this document were an initial attempt at characterizing the environment that preterm infants experience during transport and a proof that the data acquisition device collects data as expected. With the now validated data acquisition device measurements in multiple aerial and ground transports are suggested to develop a higher confidence model for each different vehicle configuration. With enough evidence that significant physical stressors are present, an IRB approval should be obtained in order to correlate the IVH cases with the stressors from the environment. Also, an IRB approval form making physical measurements of the premature babies' head is suggested to correlate those measurements with those of the environment. With the correlation, it is suggested that the current transport incubator be revised so that the new design mitigates the stressors that cause IVH. This could be as simple as a rubber absorber that has a frequency response function with a notch at 25 Hz. An acoustic dampening material between the two incubator walls that would attenuate sound levels above 500 Hz by 32 dB that could also be used to offer less exposure to light.

5.4 Summary

12 percent of babies born in the United States are born prematurely with an increasing trend as time progresses [2]. The IVH incidence in premature babies ranges from 40 to 45 percent but could be as high as 70 percent for those babies requiring mechanical ventilation [4]. Although the incidence has decrease over the past 30 years, 33 percent of premature babies who require transport are at risk for developing IVH and this incidence has not changed during the past 30 years. Several risk factors may combine to increase the overall risk for developing IVH. At the anatomical level, risk factors that cause IVH include elevated cerebral blood pressure and venous pressure, the integrity of the germinal matrix, and high fibrinolytic activity. At the physiological level, risk factors include body weight under 1.5 kg, GA under 32 weeks, and low body temperature. At the environmental level, risk factors include physical stressors such as acceleration forces, high sound levels, cold environments, and the exposure to high levels of luminance. While very little can be done for the IVH risk factors at the anatomical and physiological level, many improvements can be made to the environment that premature babies are exposed to; especially during transport from one health care facility to another. This study consisted of characterizing the environment inside and outside the transport incubator during aerial transport simultaneously. Results showed that vibrations are higher in the incubator, sound levels are well above the recommended levels, and exposure to high luminance was registered. Future work should focus on collecting more

data with the now valid data acquisition device from each aerial and ground transport in order to develop a high confidence model. Improvements to be made to the transport incubator to alleviate the IVH problem should include vibration absorbers, sound absorbing material, and sun shading material.

Bibliography

1. *Premature Birth*. 2010 November 15, 2010 [cited 2011 Sep. 9]; Available from: http://www.cdc.gov/Features/PrematureBirth/.
2. *Births by Gestational Age*. 2007 November 21, 2007 [cited 2011 9/9/2011]; Available from: http://www.cdc.gov/datastatistics/2007/births/
3. Mancini, M.C., et al., *Intraventricular hemorrhage in very low birth weight infants: associated risk factors and outcome in the neonatal period.* Rev Hosp Clin Fac Med Sao Paulo, 1999. **54**(5): p. 151-4.
4. Volpe, J.J., *Neonatal intraventricular hemorrhage.* N Engl J Med, 1981. **304**(15): p. 886-91.
5. Koksal, N., et al., *Risk factors for intraventricular haemorrhage in very low birth weight infants.* Indian J Pediatr, 2002. **69**(7): p. 561-4.
6. Yoder, B.A., *Long distance perinatal transport.* Am J Perinatol, 1992. **9**(2): p. 75-9.
7. Gleissner, M., G. Jorch, and S. Avenarius, *Risk factors for intraventricular hemorrhage in a birth cohort of 3721 premature infants.* J Perinat Med, 2000. **28**(2): p. 104-10.
8. Papile, L.A., et al., *Incidence and evolution of subependymal and intraventricular hemorrhage: a study of infants with birth weights less than 1,500 gm.* J Pediatr, 1978. **92**(4): p. 529-34.
9. McCrea, H. and L. Ment, *The Diagnosis, Management, and Postnatal Prevention of Intraventricular Hemorrhage in the Preterm Neonate.* Clinics in Perinatology, 2008. **35**(4): p. 777-792.
10. Shlossman, P.A., et al., *An analysis of neonatal morbidity and mortality in maternal (in utero) and neonatal transports at 24-34 weeks' gestation.* Am J Perinatol, 1997. **14**(8): p. 449-56.
11. Antonucci, R., A. Porcella, and V. Fanos, *The infant incubator in the neonatal intensive care unit: unresolved issues and future developments.* J Perinat Med, 2009. **37**(6): p. 587-98.
12. Sittig, S.E., et al., *Noise levels in a neonatal transport incubator in medically configured aircraft.* International Journal of Pediatric Otorhinolaryngology, 2011. **75**(1): p. 74-76.
13. Bouchut, J.C., et al., *Physical stressors during neonatal transport: helicopter compared with ground ambulance.* Air Med J, 2011. **30**(3): p. 134-9.
14. Shah, S., et al., *Quantification of impulse experienced by neonates during inter- and intra-hospital transport measured by biophysical accelerometery.* J Perinat Med, 2008. **36**(1): p. 87-92.
15. Courtney, A.C. and M.W. Courtney, *A thoracic mechanism of mild traumatic brain injury due to blast pressure waves.* Med Hypotheses, 2009. **72**(1): p. 76-83.
16. Perlman, J.M. and J.J. Volpe, *Prevention of neonatal intraventricular hemorrhage.* Clin Neuropharmacol, 1987. **10**(2): p. 126-42.

17. Shankaran, S., et al., *Sonographic classification of intracranial hemorrhage. A prognostic indicator of mortality, morbidity, and short-term neurologic outcome.* J Pediatr, 1982. **100**(3): p. 469-75.
18. Bowerman, R.A., et al., *Natural history of neonatal periventricular/intraventricular hemorrhage and its complications: sonographic observations.* AJR Am J Roentgenol, 1984. **143**(5): p. 1041-52.
19. Levene, M.I., C.L. Fawer, and R.F. Lamont, *Risk factors in the development of intraventricular haemorrhage in the preterm neonate.* Arch Dis Child, 1982. **57**(6): p. 410-7.
20. Towers, C.V., et al., *The effect of transport on the rate of severe intraventricular hemorrhage in very low birth weight infants.* Obstet Gynecol, 2000. **95**(2): p. 291-5.
21. Hohlagschwandtner, M., et al., *Perinatal mortality and morbidity. Comparison between maternal transport, neonatal transport and inpatient antenatal treatment.* Arch Gynecol Obstet, 2001. **265**(3): p. 113-8.
22. Lee, J.Y., et al., *Risk Factors for Periventricular-Intraventricular Hemorrhage in Premature Infants.* Journal of Korean Medical Science, 2010. **25**(3): p. 418.
23. Gilles, F.H., et al., *Fibrinolytic activity in the ganglionic eminence of the premature human brain.* Biol Neonate, 1971. **18**(5): p. 426-32.
24. Mori, R., et al., *Duration of inter-facility neonatal transport and neonatal mortality: systematic review and cohort study.* Pediatr Int, 2007. **49**(4): p. 452-8.
25. Li, W.G., et al., *[Effect of noise on the auditory system and the intelligence development of premature infants treated in the neonatal intensive care unit]*. Zhongguo Dang Dai Er Ke Za Zhi, 2009. **11**(12): p. 976-9.
26. Kellam, B. and J. Bhatia, *Sound Spectral Analysis in the Intensive Care Nursery: Measuring High-Frequency Sound.* Journal of Pediatric Nursing, 2008. **23**(4): p. 317-323.
27. Bremmer, P., J.F. Byers, and E. Kiehl, *Noise and the premature infant: physiological effects and practice implications.* J Obstet Gynecol Neonatal Nurs, 2003. **32**(4): p. 447-54.
28. *Atmospheric pressure and Altimetry* 2008 [cited 2011 Oct. 26, 2011]; Available from: http://www.pilotoutlook.com/aviation_weather/atmospheric_pressure_and_altimetry.
29. *Illuminance - Recommended Light Levels*. [cited 2011 Oct. 28]; Available from: http://www.engineeringtoolbox.com/light-level-rooms-d_708.html.
30. ANSI, *Preferred Frequencies, Frequency Levels, and Band Numbers for Acoustical Measurements*. 1984.
31. Orr, S.P., et al., *Physiologic responses to sudden, loud tones in monozygotic twins discordant for combat exposure: association with posttraumatic stress disorder.* Arch Gen Psychiatry, 2003. **60**(3): p. 283-8.
32. Danesi, M.A., *Photoparoxysmal discharges among patients investigated after a single seizure.* Electroencephalogr Clin Neurophysiol, 1987. **67**(6): p. 588-90.
33. Karam, O., et al., *Noise levels during nCPAP are flow-dependent but not device-dependent.* Arch Dis Child Fetal Neonatal Ed, 2008. **93**(2): p. F132-4.

Appendix A: Data Acquisition Device Schematics

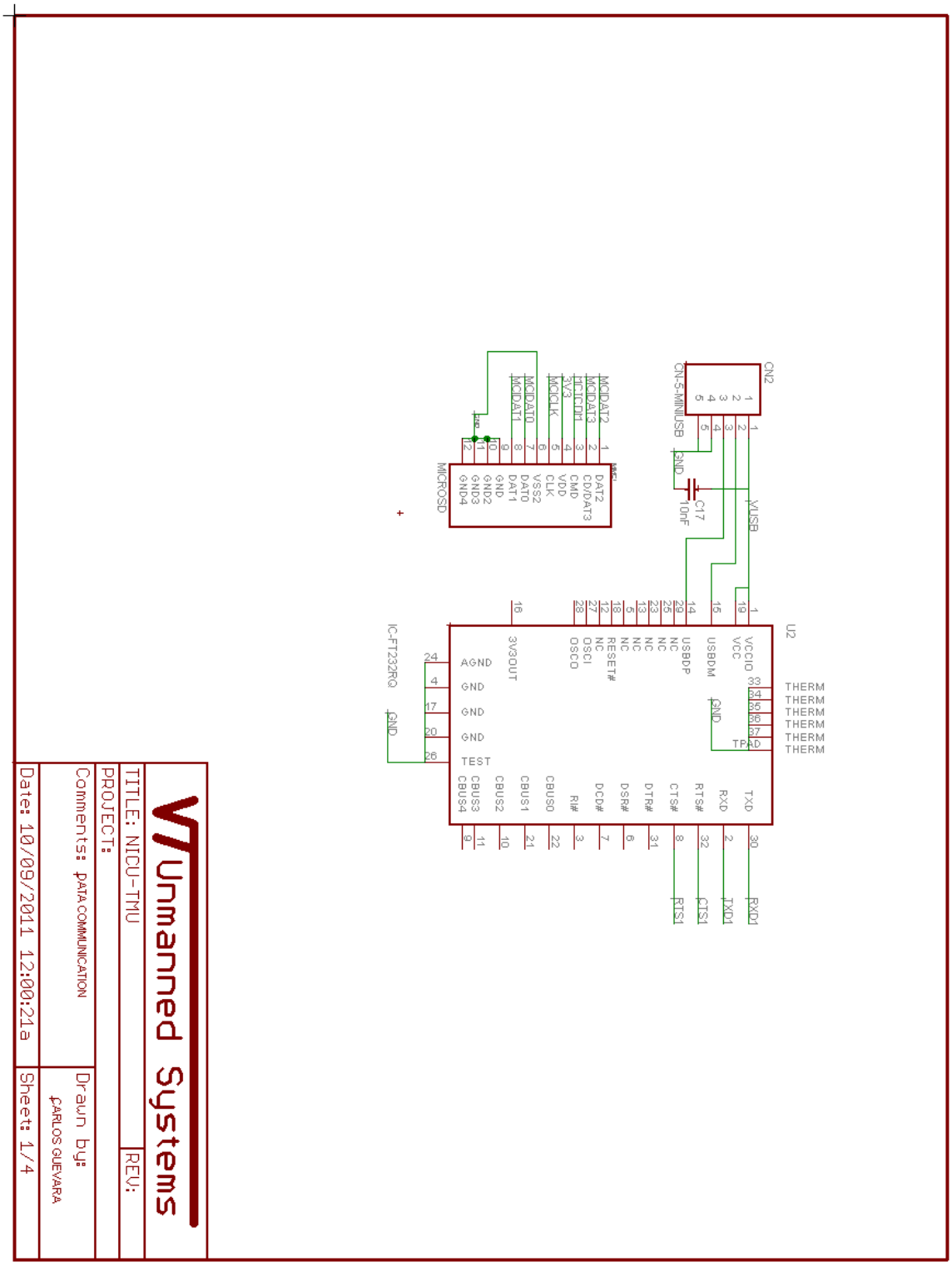

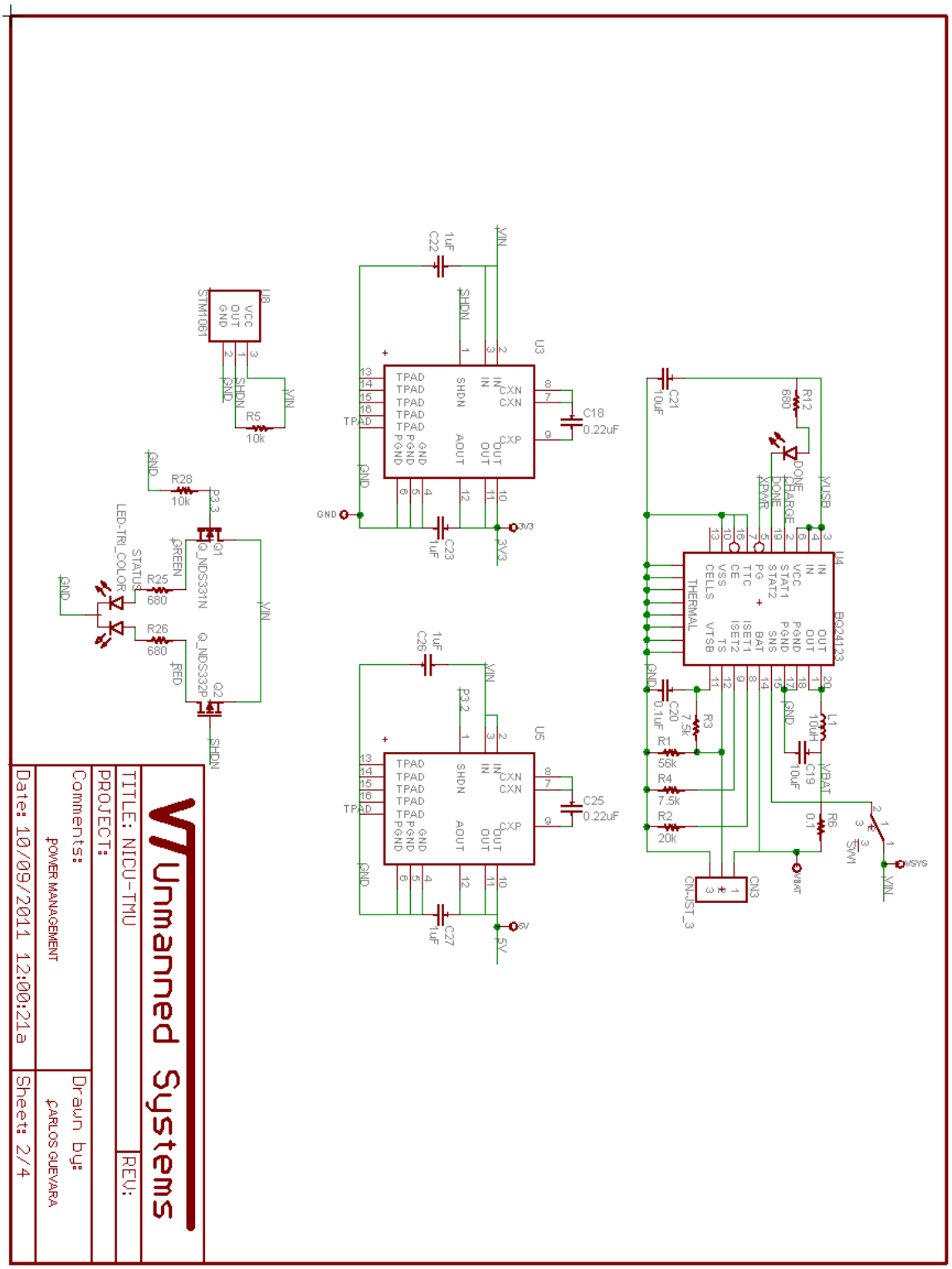
Unmanned Systems
TITLE: NICU-TMU
REV:
PROJECT:
Comments:
POWER MANAGEMENT
Drawn by:
CARLOS GUEVARA
Date: 10/09/2011 12:00:21a
Sheet: 2/4
U8
STM1061
VCC
OUT
GND
SHDN
R5
10k
VIN
C22
1uF
U3
TPAD
SHDN
IN
CXN
CXP
OUT
AOUT
PGND
C18
0.22uF
C23
1uF
3V3
R28
10k
P3.3
Q1
Q_NDS331N
GREEN
LED-TRI_COLOR
STATUS
R25
680
R26
680
RED
Q_NDS332P
Q2
C26
1uF
P3.2
U5
C25
0.22uF
C27
1uF
5V
C21
10uF
R12
680
DONE
CHARGE
XPWR
VUSB
U4
BQ24123
THERMAL
VCC
STAT1
STAT2
PG
TTC
CE
VSS
CELLS
ISET1
ISET2
TS
VTSB
BAT
SNS
C20
0.1uF
R3
7.5k
R1
56k
R4
7.5k
R2
20k
L1
10uF
C19
10uF
VBAT
R6
0.1
CN3
CON-JST_3
SW1
VSYS

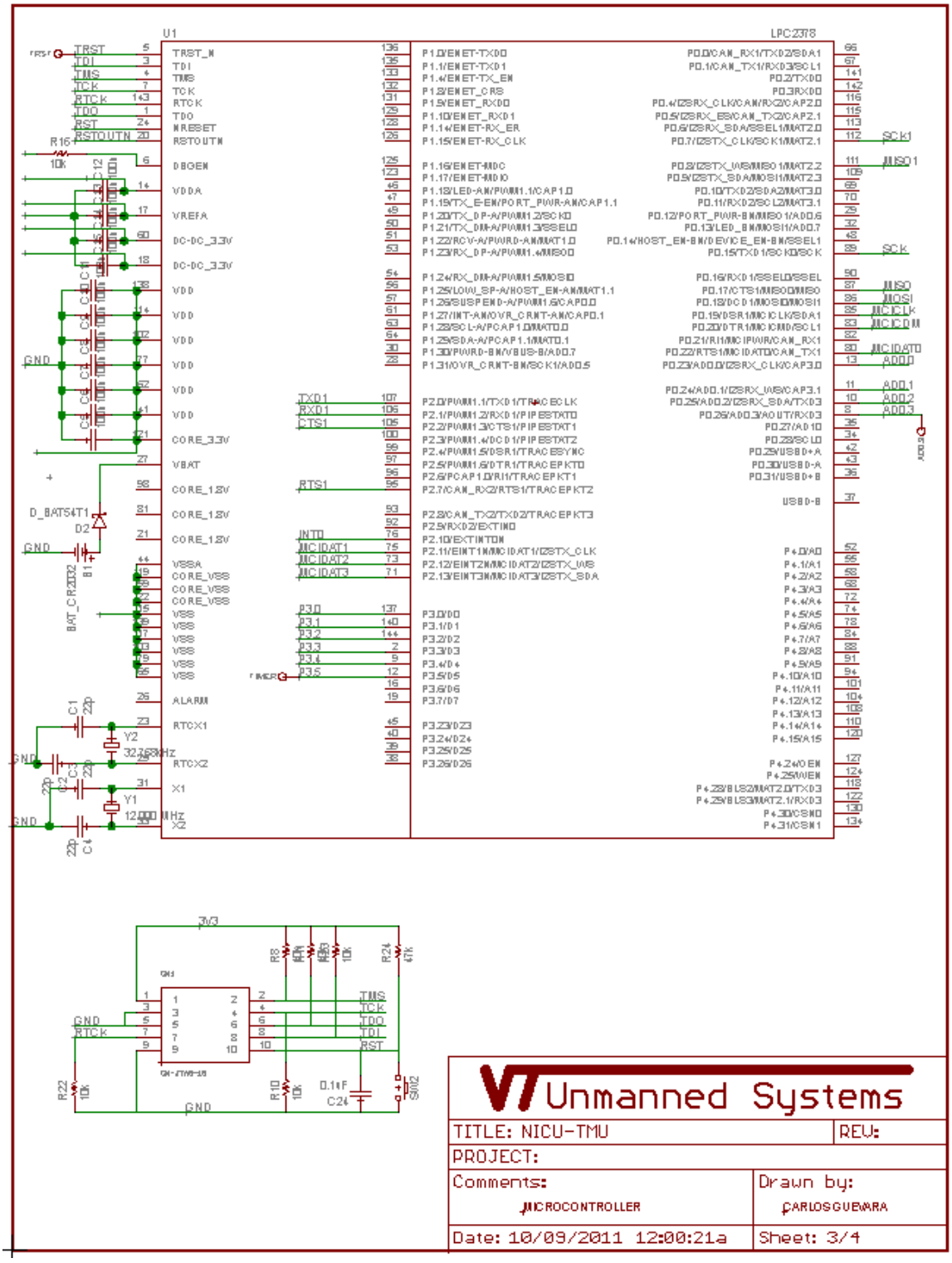

Unmanned Systems	
TITLE: NICU-TMU	REV:
PROJECT:	
Comments: MICROCONTROLLER	Drawn by: CARLOSGUEVARA
Date: 10/09/2011 12:00:21a	Sheet: 3/4

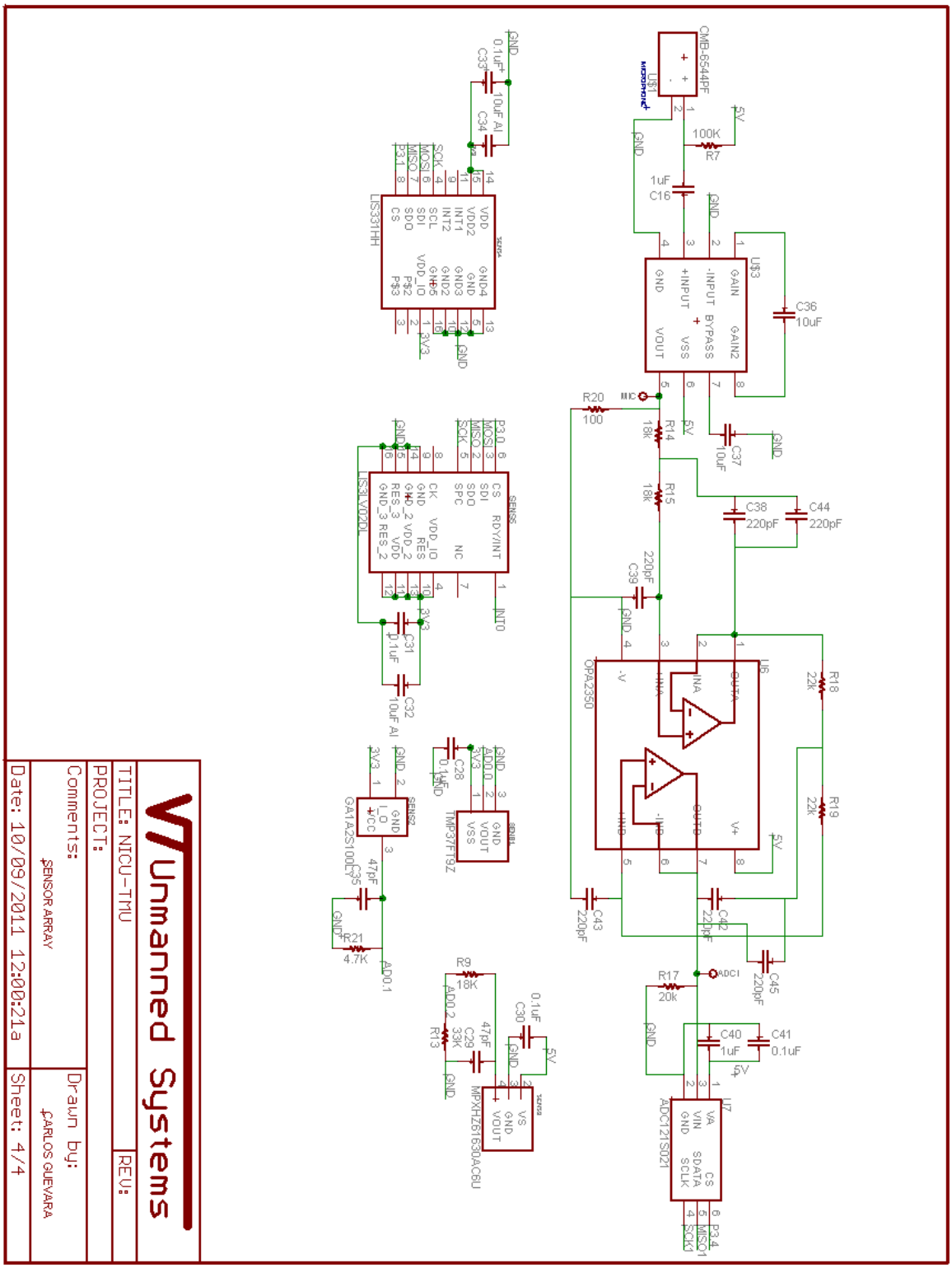
Unmanned Systems
TITLE: NICU-TMU
REV:
PROJECT:
Comments:
SENSOR ARRAY
Drawn by:
CARLOS GUEVARA
Date: 10/09/2011 12:00:21a
Sheet: 4/4

Appendix B: Microcontroller and Transducer Specifications

LPC2377/78

Single-chip 16-bit/32-bit microcontrollers; 512 kB flash with ISP/IAP, Ethernet, USB 2.0, CAN, and 10-bit ADC/DAC

Rev. 5 — 17 June 2010 Product data sheet

1. General description

The LPC2377/78 microcontrollers are based on a 16-bit/32-bit ARM7TDMI-S CPU with real-time emulation that combines the microcontroller with 512 kB of embedded high-speed flash memory. A 128-bit wide memory interface and a unique accelerator architecture enable 32-bit code execution at the maximum clock rate. For critical performance in interrupt service routines and DSP algorithms, this increases performance up to 30 % over Thumb mode. For critical code size applications, the alternative 16-bit Thumb mode reduces code by more than 30 % with minimal performance penalty.

The LPC2377/78 are ideal for multi-purpose serial communication applications. It incorporates a 10/100 Ethernet Media Access Controller (MAC), USB full speed device with 4 kB of endpoint RAM (LPC2378 only), four UARTs, two CAN channels (LPC2378 only), an SPI interface, two Synchronous Serial Ports (SSP), three I^2C-bus interfaces, an I^2S-bus interface, and an External Memory Controller (EMC). This blend of serial communications interfaces combined with an on-chip 4 MHz internal oscillator, SRAM of 32 kB, 16 kB SRAM for Ethernet, 8 kB SRAM for USB and general purpose use, together with 2 kB battery powered SRAM make this device very well suited for communication gateways and protocol converters. Various 32-bit timers, an improved 10-bit ADC, 10-bit DAC, PWM unit, a CAN control unit, and up to 104 fast GPIO lines with up to 50 edge and up to four level sensitive external interrupt pins make these microcontrollers particularly suitable for industrial control and medical systems.

2. Features and benefits

- ARM7TDMI-S processor, running at up to 72 MHz.
- Up to 512 kB on-chip flash program memory with In-System Programming (ISP) and In-Application Programming (IAP) capabilities. Flash program memory is on the ARM local bus for high performance CPU access.
- 32 kB of SRAM on the ARM local bus for high performance CPU access.
- 16 kB SRAM for Ethernet interface. Can also be used as general purpose SRAM.
- 8 kB SRAM for general purpose DMA use also accessible by the USB.
- Dual Advanced High-performance Bus (AHB) system that provides for simultaneous Ethernet DMA, USB DMA, and program execution from on-chip flash with no contention between those functions. A bus bridge allows the Ethernet DMA to access the other AHB subsystem.
- EMC provides support for static devices such as flash and SRAM as well as off-chip memory mapped peripherals.
- Advanced Vectored Interrupt Controller (VIC), supporting up to 32 vectored interrupts.

LIS3LV02DL

MEMS inertial sensor
3-axis - ±2g/±6g digital output low voltage linear accelerometer

Features

- 2.16 V to 3.6 V single supply operation
- 1.8 V compatible IOs
- I^2C/SPI digital output interfaces
- Programmable 12 or 16 bit data representation
- Interrupt activated by motion
- Programmable interrupt threshold
- Embedded self test
- High shock survivability
- ECOPACK® compliant (see *Section 9*)

LGA-16

Description

The LIS3LV02DL is a three axes digital output linear accelerometer that includes a sensing element and an IC interface able to take the information from the sensing element and to provide the measured acceleration signals to the external world through an I^2C/SPI serial interface.

The sensing element, capable of detecting the acceleration, is manufactured using a dedicated process developed by ST to produce inertial sensors and actuators in silicon.

The IC interface instead is manufactured using a CMOS process that allows high level of integration to design a dedicated circuit which is factory trimmed to better match the sensing element characteristics.

The LIS3LV02DL has a user selectable full scale of ±2g, ±6g and it is capable of measuring acceleration over a bandwidth of 640 Hz for all axes. The device bandwidth may be selected accordingly to the application requirements.

The self-test capability allows the user to check the functioning of the device.

The device may be also configured to generate an inertial wake-up/free-fall interrupt signal when a programmable acceleration threshold is crossed at least in one of the three axes.

The LIS3LV02DL is available in plastic SMD package and it is specified over a temperature range extending from -40°C to +85°C.

The LIS3LV02DL belongs to a family of products suitable for a variety of applications:

- Free-Fall detection
- Motion activated functions in portable terminals
- Antitheft systems and Inertial navigation
- Gaming and virtual reality input devices
- Vibration monitoring and compensation

Table 1. Device summary

Order code	Operating temperature range [° C]	Package	Packing
LIS3LV02DL	-40 to +85	LGA-16	Tray
LIS3LV02DLTR	-40 to +85	LGA-16	Tape and reel

PART NUMBER: CMB-6544PF **DESCRIPTION:** electret condenser microphone

SPECIFICATIONS

directivity	omnidirectional	
sensitivity (S)	-44 ±3 dB	f = 1KHz, 1Pa 0dB = 1V/Pa
sensitivity reduction (ΔS-Vs)	-3 dB	f = 1KHz, 1Pa Vs = 4.5 ~ 1.5 V dc
operating voltage	4.5 V dc (standard), 10 V dc (max.)	
output impedance (Zout)	1 KΩ	f = 1KHz, 1Pa
operating frequency (f)	20 ~ 20,000 Hz	
current consumption (Idss)	0.5 mA max.	Vs = 4.5 V dc RL = 1KΩ
signal to noise ratio (S/N)	60 dBA	f = 1KHz, 1Pa A-weighted
operating temperature	-20 ~ +70° C	
storage temperature	-20 ~ +70° C	
dimensions	ø9.4 x 6.5 mm	
weight	0.7 g max.	
material	Al	
terminal	pin type (hand soldering only)	
RoHS	yes	

note: We use the "Pascal (Pa)" indication of sensitivity as per the recomendation of I.E.C. (International Electrotechnical Commission). The sensitivity of "Pa" will increase 20dB compared to the "ubar" indication. Example: -60dB (0dB = 1V/ubar) = -40dB (1V/Pa)

APPEARANCE DRAWING

tolerances not shown: ±0.3mm

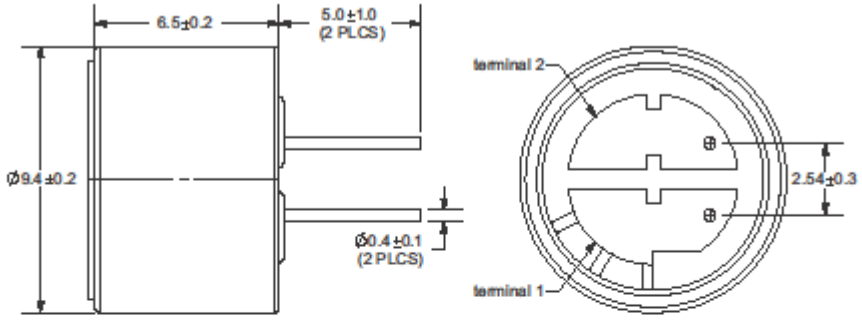

Low Voltage Temperature Sensors

TMP35/TMP36/TMP37

FEATURES

Low voltage operation (2.7 V to 5.5 V)
Calibrated directly in °C
10 mV/°C scale factor (20 mV/°C on TMP37)
±2°C accuracy over temperature (typ)
±0.5°C linearity (typ)
Stable with large capacitive loads
Specified −40°C to +125°C, operation to +150°C
Less than 50 µA quiescent current
Shutdown current 0.5 µA max
Low self-heating

APPLICATIONS

Environmental control systems
Thermal protection
Industrial process control
Fire alarms
Power system monitors
CPU thermal management

GENERAL DESCRIPTION

The TMP35/TMP36/TMP37 are low voltage, precision centigrade temperature sensors. They provide a voltage output that is linearly proportional to the Celsius (centigrade) temperature. The TMP35/ TMP36/TMP37 do not require any external calibration to provide typical accuracies of ±1°C at +25°C and ±2°C over the −40°C to +125°C temperature range.

The low output impedance of the TMP35/TMP36/TMP37 and its linear output and precise calibration simplify interfacing to temperature control circuitry and ADCs. All three devices are intended for single-supply operation from 2.7 V to 5.5 V maximum. The supply current runs well below 50 µA, providing very low self-heating—less than 0.1°C in still air. In addition, a shutdown function is provided to cut the supply current to less than 0.5 µA.

The TMP35 is functionally compatible with the LM35/LM45 and provides a 250 mV output at 25°C. The TMP35 reads temperatures from 10°C to 125°C. The TMP36 is specified from −40°C to +125°C, provides a 750 mV output at 25°C, and operates to 125°C from a single 2.7 V supply. The TMP36 is functionally compatible with the LM50. Both the TMP35 and TMP36 have an output scale factor of 10 mV/°C.

FUNCTIONAL BLOCK DIAGRAM

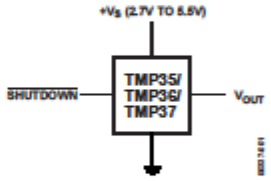

Figure 1.

PIN CONFIGURATIONS

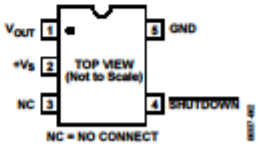

Figure 2. RJ-5 (SOT-23)

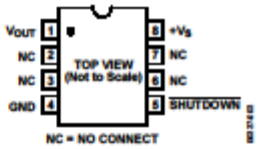

Figure 3. R-8 (SOIC_N)

Figure 4. T-3 (TO-92)

The TMP37 is intended for applications over the range of 5°C to 100°C and provides an output scale factor of 20 mV/°C. The TMP37 provides a 500 mV output at 25°C. Operation extends to 150°C with reduced accuracy for all devices when operating from a 5 V supply.

The TMP35/TMP36/TMP37 are available in low cost 3-lead TO-92, 8-lead SOIC_N, and 5-lead SOT-23 surface-mount packages.

One Technology Way, P.O. Box 9106, Norwood, MA 02062-9106, U.S.A.
Tel: 781.329.4700 www.analog.com
Fax: 781.461.3113

Freescale Semiconductor

MPXA6115A
Rev 6, 06/2010

High Temperature Accuracy Integrated Silicon Pressure Sensor for Measuring Absolute Pressure, On-Chip Signal Conditioned, Temperature Compensated and Calibrated

MPXA6115A
MPXAZ6115A
MPXH6115A
MPXHZ6115A
Series
15 to 115 kPa (2.2 to 16.7 psi)
0.2 to 4.8 V Output

The MPXxx6115A series sensor integrates on-chip, bipolar op amp circuitry and thin film resistor networks to provide a high output signal and temperature compensation. The small form factor and high reliability of on-chip integration make the pressure sensor a logical and economical choice for the system designer.

The MPXxx6115A series piezoresistive transducer is a state-of-the-art, monolithic, signal conditioned, silicon pressure sensor. This sensor combines advanced micromachining techniques, thin film metallization, and bipolar semiconductor processing to provide an accurate, high level analog output signal that is proportional to applied pressure.

Application Examples

- Aviation Altimeters
- Industrial Controls
- Engine Control/Manifold Absolute Pressure (MAP)
- Weather Station and Weather Reporting Device Barometers

Features

- Resistant to High Humidity and Common Automotive Media
- Improved Accuracy at High Temperature
- Available in Small and Super Small Outline Packages
- 1.5% Maximum Error over 0° to 85°C
- Ideally suited for Microprocessor or Microcontroller-Based Systems
- Temperature Compensated from -40° to +125°C
- Durable Thermoplastic (PPS) Surface Mount Package

ORDERING INFORMATION

Device Name	Case No.	# of Ports			Pressure Type			Device Marking
		None	Single	Dual	Gauge	Differential	Absolute	
Small Outline Package (MPXA6115A Series)								
MPXA6115A6U	482	•					•	MPXA6115A
MPXA6115A6T1	482	•					•	MPXA6115A
MPXA6115AC6U	482A		•				•	MPXA6115A
MPXA6115AC6T1	482A		•				•	MPXA6115A
MPXA6115AC7U	482C		•				•	MPXA6115A
Small Outline Package (Media Resistant Gel) (MPXAZ6115A Series)								
MPXAZ6115A6U	482	•					•	MPXAZ6115A
MPXAZ6115AC6U	482A		•				•	MPXAZ6115A
MPXAZ6115AC6T1	482A		•				•	MPXAZ6115A
MPXAZ6115AP	1369		•				•	MPXAZ6115A
MPXAZ6115APT1	1369		•				•	MPXAZ6115A
Super Small Outline Package (MPXH6115A Series)								
MPXH6115A6U	1317	•					•	MPXH6115A
MPXH6115A6T1	1317	•					•	MPXH6115A
MPXH6115AC6U	1317A		•				•	MPXH6115A
MPXH6115AC6T1	1317A		•				•	MPXH6115A

GA1A2S100SS/ GA1A2S100LY

OPIC™ Linear Output Ambient Light Sensor

■ Features

1. Linear output, suitable for indoor or outdoor use
2. Light sensitivity and response curve similar to that of the human eye
3. OPIC light detector: integrated photodiode and signal processing circuit
4. Lead frame packages:
   Straight leads: GA1A2S100SS
   L-bend: GA1A2S100LY
5. Stable over specified temperature range
6. Lead-free and RoHS-directive compliant

■ Agency Approvals/Compliance

1. Compliant with RoHS directive (2002/95/EC)
2. Content information about the six substances specified in "Management Methods for Control of Pollution Caused by Electronic Information Products Regulation" (popular name: China RoHS) (Chinese: 电子信息产品污染控制管理办法); refer to page 7.

■ Applications

1. Auto-dimming circuits
2. Office automation equipment
3. Audio visual equipment
4. Home appliances
5. Touch panels

OPIC is a trademark of Sharp Corporation.

Sheet No.: D1-A00501EN
Date: October 1, 2007

Appendix C: Digital Filter Design Code

```
clear all
close all
clc
% Digital Filter design
%frequency bands per ANSI S1.6-1984

n = 12:44; % band number
fc = 10.^(n./10); % exact center frequency
B = 0.231*fc; %bandwidth per band
HB = B./2; % half bandwidht
%----------------  Filter Specifications -------------------------
PB = [fc-HB; fc+HB]'; % pass band array
Ap = 2.6; % Passband ripple in dB
As = 30; % Stopband ripple in dB
Fs = 51200; % sampling frequency in Hz
Fn = Fs/2;
%fr = logspace(0,5,4096);

%--------------------- Filter Design ----------------------------

q = quantizer('nearest',[15 14]);
coefmatraw =zeros(3,5);

for i = 2:length(PB)-1

    [N, wc] = ellipord(PB(i,:)/Fn, [fc(i-1)/Fn, 0.95*fc(i+1)/Fn], Ap,
As); %specify filter order
    [z,p,k] = ellip(N,Ap,As,wc); % poles and zeros
    [sos] = zp2sos(z,p,k); % second order sections of the filters
    sosq = num2int(q,sos./4);

    coefmatraw = [coefmatraw; sosq(:,1) sosq(:,2) sosq(:,3) sosq(:,5)
sosq(:,6)];
    h(i-1) = dfilt.df1sos(sos); % filter models
    hq(i-1) = dfilt.df1sos(sosq);


end

coefmat = [coefmatraw(4:96,:)];
dlmwrite('coefmatrix.txt',coefmat, 'precision', '%d')

%freqz(h) % floating point filter FRF
freqz(hq) % fixed point filter FRF

%--------------------- Filter Simulation -------------------------

% f1 = 20; % input signal 1 at 20 Hz
% f2 = 100; % input signal 2 at 100 Hz
% tau1 = 1/f1; % period of the input signal
% tau2 = 1/f2;
% % Characteristics of the DAQ's ADC
```

```
% Fs = 50240; %Sampling at 60 KHz
% Ts = 1/Fs; % Sample period
% Tf = 1.5; % duration of the signal in seconds
%
% [x1,t] = gensig('sin',tau1,Tf,Ts);
% [x2,t] = gensig('sin',tau2,Tf,Ts);
% x = (x2+x1)/2;
% y = filter(h(13),x);
%
% figure
% stairs(t,x)
% hold off
% stairs(t,y,'r')
% ylabel('Amplitude')
% xlabel('Time (s)')


% subplot(211)
% semilogx(fr,20*log10(abs(frf)))
% grid on
% ylabel('Magnitude (dB)')
% subplot(212)
% semilogx(fr,(180/pi)*angle(frf))
% grid on
% ylabel('Phase (deg)')
% xlabel('Frequency (Hz)')
```

Appendix D: LabVIEW Code

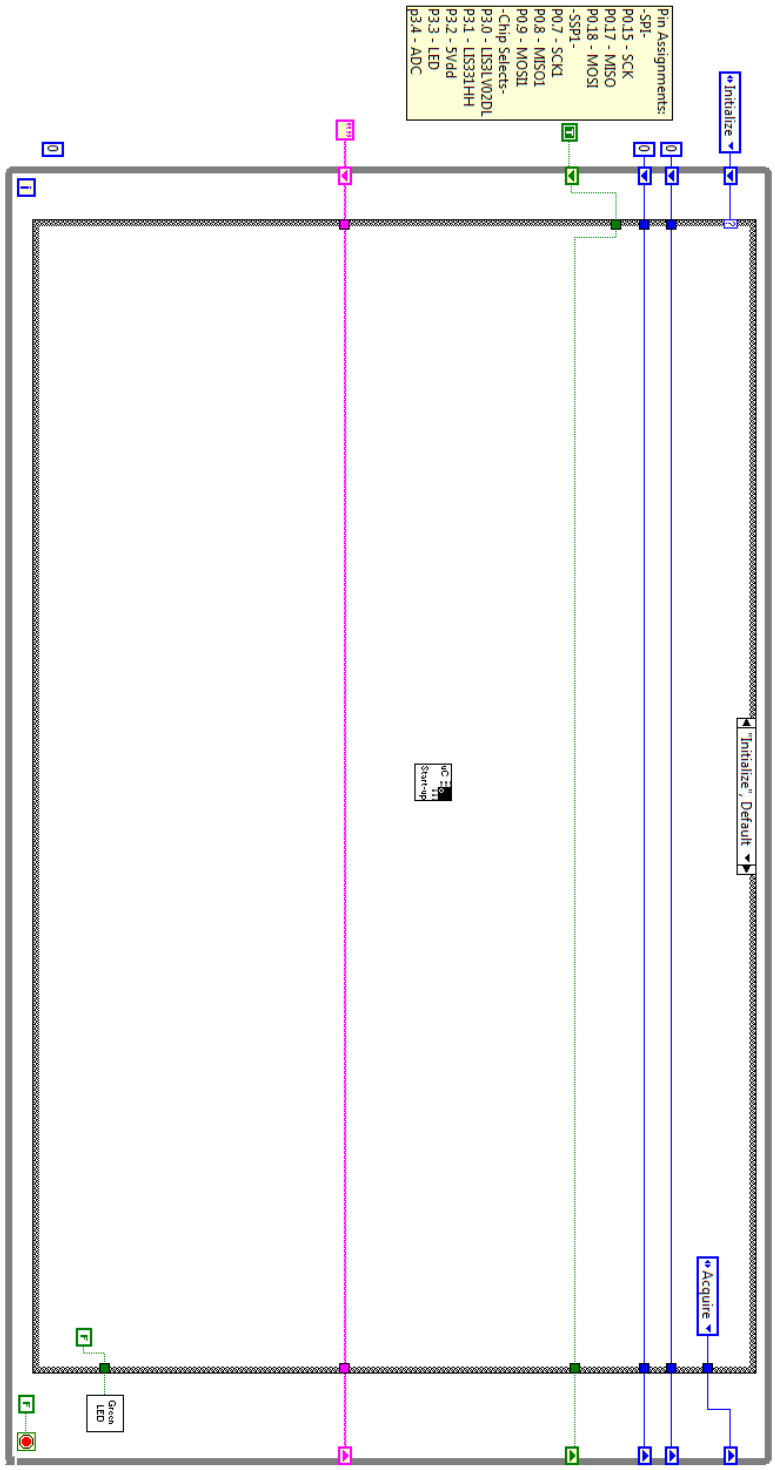

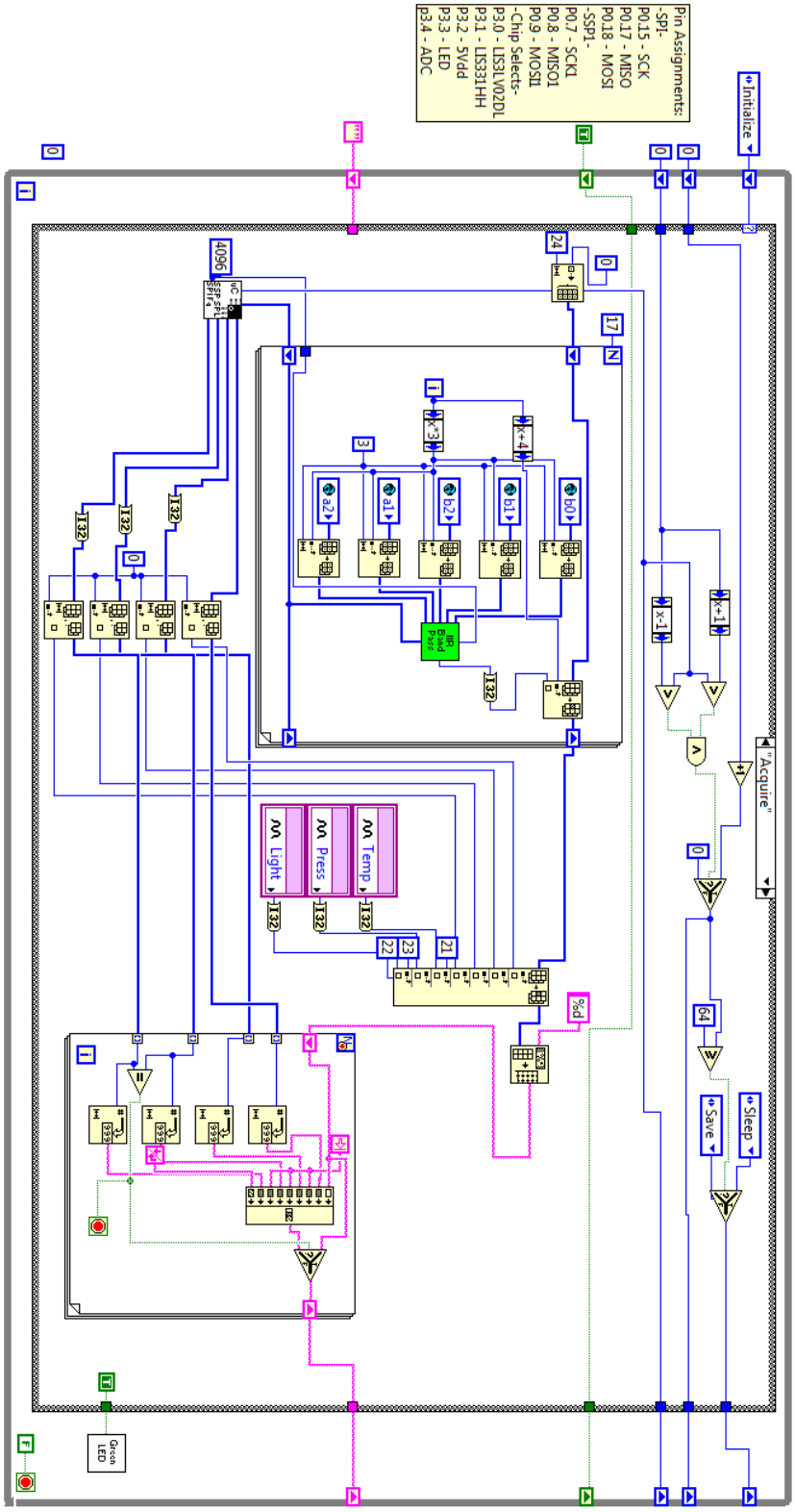
Pin Assignments:
-SPI-
P0.15 - SCK
P0.17 - MISO
P0.18 - MOSI
-SSP1-
P0.7 - SCK1
P0.8 - MISO1
P0.9 - MOSI1
-Chip Selects-
P3.0 - LIS3LV02DL
P3.1 - LIS331HH
P3.2 - 5Vdd
P3.3 - LED
p3.4 - ADC
Initialize
"Acquire"
Light
Press
Temp
Save
Sleep
Green LED

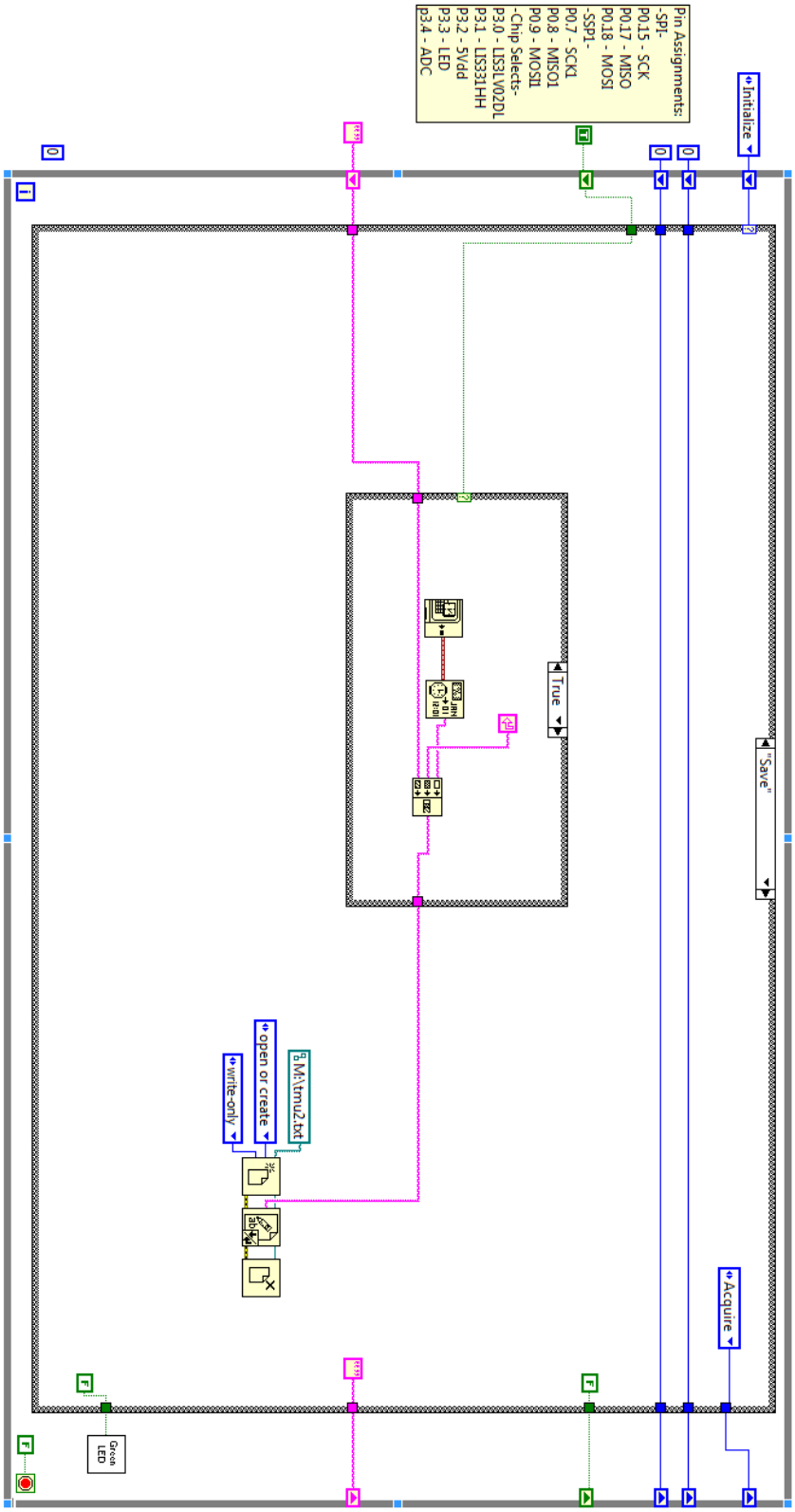
Pin Assignments:
-SPI-
P0.15 - SCK
P0.17 - MISO
P0.18 - MOSI
-SSP1-
P0.7 - SCK1
P0.8 - MISO1
P0.9 - MOSI1
-Chip Selects-
P3.0 - LIS3LV02DL
P3.1 - LIS331HH
P3.2 - 5Vdd
P3.3 - LED
p3.4 - ADC
Initialize
True
"Save"
open or create
write-only
B:\M:\tmu2.txt
Acquire
Green LED

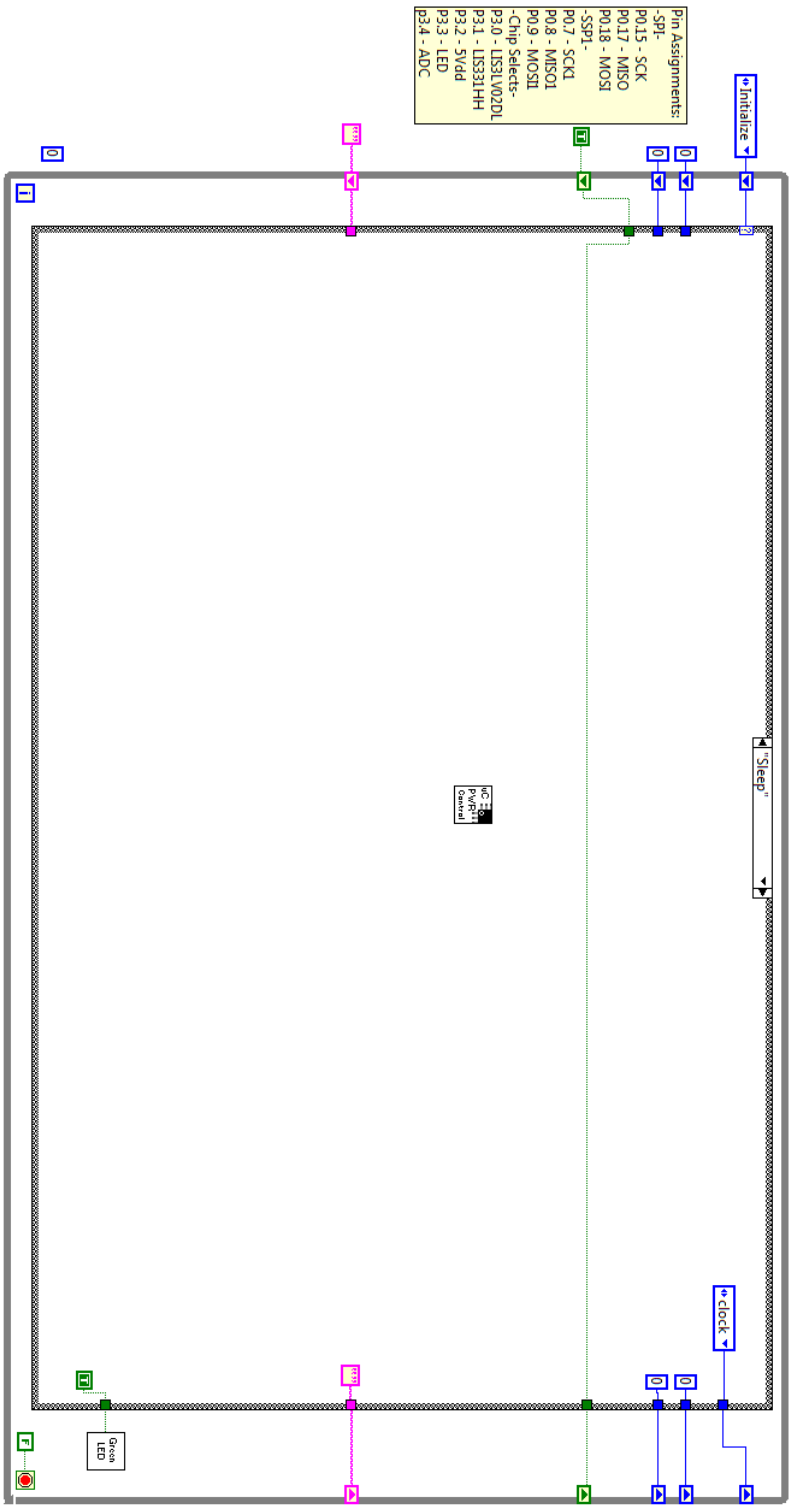
Pin Assignments:
-SPI-
P0.15 - SCK
P0.17 - MISO
P0.18 - MOSI
-SSP1-
P0.7 - SCK1
P0.8 - MISO1
P0.9 - MOSI1
-Chip Selects-
P3.0 - LIS3LV02DL
P3.1 - LIS331HH
P3.2 - 5Vdd
P3.3 - LED
p3.4 - ADC
Initialize
"Sleep"
clock
Green LED

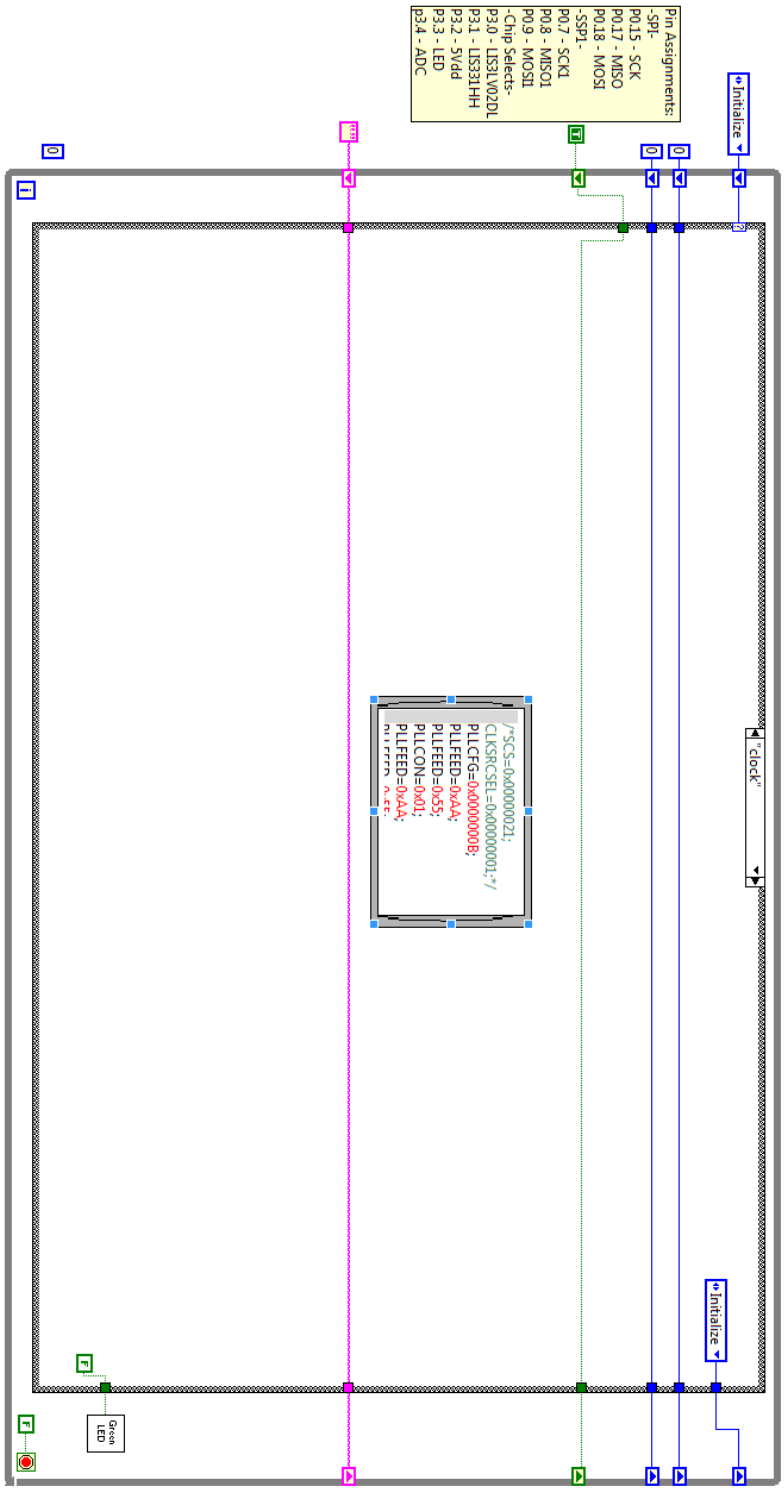
Pin Assignments:
-SPI-
P0.15 - SCK
P0.17 - MISO
P0.18 - MOSI
-SSP1 -
P0.7 - SCK1
P0.8 - MISO1
P0.9 - MOSI1
-Chip Selects-
P3.0 - LIS3LV02DL
P3.1 - LIS331HH
P3.2 - 5Vdd
P3.3 - LED
p3.4 - ADC
Initialize
"clock"
Green LED
Initialize

Appendix E: Batch Signal Processing Matlab Code

```
clear all
close all
clc

SDcomp = importdata('TMU1AIR.TXT'); % load raw data from uSD card
Date = getfield(SDcomp,'textdata'); % extract the date header
data = getfield(SDcomp,'data'); % extract data
fc = [125 250 500 1000 1250 1600 2000 2500 3150 4000 5000 6300 8000
10000 ...
      12500 16000 20000]; % specify filter bank center frequency
Aw = [-16.1 -8.6 -3.2 0 0.6 1 1.2 1.3 1.2 1 0.5 -0.1 -1.1 -2.5 -4.3 -
6.6 -9.3];
% Aw are the weights for the A-weighted sound measurement

%--------
t = uint32(data(:,1));

for i = 1:length(t) % extract HH:MM:SS from raw time stamp

    d(i) = (bin2dec(num2str(bitget(t(i),27:-1:25))));
    h(i) = (bin2dec(num2str(bitget(t(i),21:-1:17))));
    m(i) = (bin2dec(num2str(bitget(t(i),14:-1:9))));
    s(i) = bin2dec(num2str(bitget(t(i),6:-1:1)));
end

yy = 2011; mm = 07; % year and month set manually for now
yy = yy*ones(length(t),1);
mm = mm*ones(length(t),1);
V = [yy mm (d+1)' h' m' s']; % create time stamp vector
tstamp = datenum(V); % convert to matlab time stamp format
t = h+m+s;
x = (data(:,2))./340; % convert raw accelerometer reading to G's
y = (data(:,3))./340;
z = (data(:,4))./340;
x = x-mean(x);
y = y-mean(y);
z = z-mean(z); % remove the ofset induced by gravity
SPL = data(:,5:21); % extract raw sound data
Tb = data(:,22); % extract raw temperature data
Pb = data(:,23); % extract raw pressure data
Lb = data(:,24); % extract war luminance data
tstamps = tstamp; % create a time stamp to match the SPL, Tb, Pb, Lb
length

%-----------------  remove the white space --------------------------
----
SPL(any(isnan(SPL),2),:)=[];
tstamps(isnan(Pb)) = [];
Tb(isnan(Tb)) = [];
Pb(isnan(Pb)) = [];
Lb(isnan(Lb)) = [];
%-------------------------------------------------------------------
----
```

```
VSPLrms = abs(sqrt(abs(SPL)*(5/4096)^2)); % compute sound rms
dBSPL = 20*log10(((VSPLrms/200)/0.0063)/(20*10^-6)); % scale sound data
AdBSPL = zeros(size(dBSPL));
for j = 1:17 % fit sound data with the A-weighted curve
    AdBSPL(:,j) = dBSPL(:,j) + Aw(j);
end


Temp = (165/1024).*Tb; % scale temperature data
Press = ((((51/33).*(3.3/1024).*Pb)/5)+0.095)/0.009; % scale pressure
data
Light = (10095.44787/1024).*Lb; % scale luminance data

for k = 1:length(Temp) % remove temperature zeros
    if Temp(k) < 10
        Temp(k) = (Temp(k-1)+Temp(k+1))/2;
    else
        Temp(k) = Temp(k);
    end
end

%------------------ acceleration vs time plots -----------------------
----
subplot(311)
plot(tstamp,x)
datetick('x',14,'keepticks')
title('Acceleration in X axis')
ylim([-2 5])
xlim([7.346884441550926e+05 7.346884806365741e+05])
ylabel('Gs')
grid on
subplot(312)
plot(tstamp,y)
datetick('x',14,'keepticks')
title('Acceleration inY axis')
ylim([-2 5])
xlim([7.346884441550926e+05 7.346884806365741e+05])
ylabel('Gs')
grid on
subplot(313)
plot(tstamp,z)
datetick('x',14,'keepticks')
title('Acceleration in Z axis')
ylim([-2 5])
xlim([7.346884441550926e+05 7.346884806365741e+05])
ylabel('Gs')
grid on

% -------------- Sound spectrogram plot ------------------------------
----
figure
contourf(tstamps,1:17,AdBSPL', 'edgecolor','none'); axis tight;
colormap(jet(16));
caxis([30 90])
colorbar('YTickLabel',...
```

```
    {'30dBA - Quiet residence','40dBA - Soft stereo','50dBA', ...
    '60dBA - Speech range','70dBA','80dBA - Cafeteria','90dBA -
Jackhammer'})
view(0,90);
datetick('x',14,'keepticks')
set(gca,'YTick',1:17)
set(gca,'YGrid','on')
set(gca,'YTickLabel',{125 250 500 1000 1250 1600 2000 2500 3150 4000
5000 6300 8000 10000 ...
      12500 16000 20000})
xlim([7.346884441550926e+05 7.346884806365741e+05])
title('Sound Spectral Analysis')
xlabel('Time')
ylabel('Center Frequency (Hz)')
zlabel('SPL (dB)')

% --------- Temperature pressure and luminance plots ------------------
----
figure
%subplot(311)
plot(tstamps,Temp); axis tight;
annotation('textbox',[0.63 0.6 0.25 0.3],'BackgroundColor','w','String'
...
    ,{'Mean Temp:',num2str(mean(Temp),3),'Max
Temp:',num2str(max(Temp),3) ...
    ,'Standard Deviation:',num2str(std(Temp),3)})
datetick('x',14,'keepticks')
title('Temperature')
ylim([20 50])
xlim([7.346884441550926e+05 7.346884806365741e+05])
ylabel('C\circ')
xlabel('Time')
grid on

figure%subplot(312)
plot(tstamps,Press+3); axis tight;
annotation('textbox',[0.63 0.6 0.25 0.3],'BackgroundColor','w','String'
...
    ,{'Mean Press:',num2str(mean(Press+3),4),'Max
Press:',num2str(max(Press+3),4) ...
    ,'Standard Deviation:',num2str(std(Press+3),4)})
datetick('x',14,'keepticks')
title('Pressure')
ylim([80 105])
xlim([7.346884441550926e+05 7.346884806365741e+05])
ylabel('kPa')
xlabel('Time')
grid on

figure%subplot(313)
semilogy(tstamps,Light); axis tight;
annotation('textbox',[0.63 0.6 0.25 0.3],'BackgroundColor','w','String'
...
    ,{'Mean Lux:',num2str(mean(Light),3),'Max
Lux:',num2str(max(Light),3) ...
    ,'Standard Deviation:',num2str(std(Light),3)})
```

```
datetick('x',14,'keepticks')
title('Luminance')
ylim([100 10000])
xlim([7.346884441550926e+05 7.346884806365741e+05])
ylabel('Lux')
xlabel('Time')
grid on

% -------- set the requirements for spectrogram function -------------
----
Fs = 160;
L = length(z);
%NFFT = 2^nextpow2(L/4);
SFFT = 2^10; % length of the short FFT

tstampsa = tstamp(SFFT:5:length(x));

% ----------- FFT used to calibrate the accelerometer -----------------
----
% Z = fft(z,NFFT)/L;
% f = Fs/2*linspace(0,1,NFFT/2+1);
%
% figure
% plot(f,2*abs(Z(1:NFFT/2+1)))
% title('DFT of the accelerometer response')
% ylabel('Gs - Z-axis')
% xlabel('frequency (Hz)')
% ylim([0 0.1])
% xlim([0 80])
% grid on

% -------- Vibration spectrograms and histogram plots ----------------
----
[S,F,T,P] = spectrogram(x,SFFT,SFFT-5,SFFT,Fs);
figure
surf(tstampsa,F,9.81*2*abs(S(1:SFFT/2+1,:)/SFFT),'edgecolor','none');
axis tight;
colormap(jet(128));
caxis([0 0.25])
colorbar
view(0,90);
set(gca,'XScale','log')
set(gca,'YGrid','on')
datetick('x',14,'keepticks')
xlim([7.346884441550926e+05 7.346884803472222e+05])
title('X-axis Vibration Spectrogram (m/s^2)')
ylabel('Frequencies (Hz)')
xlabel('Time')

[S,F,T,P] = spectrogram(y,SFFT,SFFT-5,SFFT,Fs);
figure
surf(tstampsa,F,9.81*2*abs(S(1:SFFT/2+1,:)/SFFT),'edgecolor','none');
axis tight;
colormap(jet(128));
caxis([0 0.25])
colorbar
```

```
view(0,90);
set(gca,'XScale','log')
set(gca,'YGrid','on')
datetick('x',14,'keepticks')
xlim([7.346884441550926e+05 7.346884803472222e+05])
title('Y-axis Vibration Spectrogram (m/s^2)')
ylabel('Frequencies (Hz)')
xlabel('Time')

[S,F,T,P] = spectrogram(z,SFFT,SFFT-5,SFFT,Fs);
figure
surf(tstampsa,F,9.81*2*abs(S(1:SFFT/2+1,:)/SFFT),'edgecolor','none');
axis tight;
colormap(jet(128));
caxis([0 0.25])
colorbar
view(0,90);
set(gca,'XScale','log')
set(gca,'YGrid','on')
datetick('x',14,'keepticks')
xlim([7.346884441550926e+05 7.346884803472222e+05])
title('Z-axis Vibration Spectrogram (m/s^2)')
ylabel('Frequencies (Hz)')
xlabel('Time')
```